Topological connection between vesicles and nanotubes in single-component lipid membranes driven by head-tail interactions

Niki Baccile, Cédric Lorthioir, Abdoul Aziz Ba, Patrick Le Griel, Cristina Coelho Diogo, Javier Perez, Wim Soetaert, Sophie L K W Roelants

Topological connection between vesicles and nanotubes in single-component lipid membranes driven by head-tail interactions

Niki Baccile,[a,*] Cédric Lorthioir,[a] Abdoul Aziz Ba,[a] Patrick Le Griel,[a] Cristina Coelho Diogo,[b] Javier Perez,[c] Wim Soetaert,[d] Sophie L. K. W. Roelants[d]

[a] Sorbonne Université, Centre National de la Recherche Scientifique, Laboratoire de Chimie de la Matière Condensée de Paris, LCMCP, F-75005 Paris, France

[b] Institut des Matériaux de Paris Centre, Sorbonne Université, Paris, France

[c] Synchrotron Soleil, L'Orme des Merisiers, Saint-Aubin, BP48, 91192 Gif-sur-Yvette Cedex, France

[d] InBio, Department of Biotechnology, Ghent University, Ghent, Belgium

*** Corresponding author:**

Dr. Niki Baccile

E-mail address: niki.baccile@sorbonne-universite.fr

Phone: +33 1 44 27 56 77

Abstract

Lipid nanotube-vesicle networks are important channels for intercellular communication and transport of matter. Experimentally observed in neighboring mammalian cells, but also reproduced in model membrane systems, a broad consensus exists on their formation and stability. Lipid membranes must be composed of at least two components, each stabilizing low (generally a phospholipid) and high curvatures. Strong anisotropy or enhanced conical shape of the second amphiphilic component is crucial for the formation of nanotunnels. Anisotropic driving forces generally favor nanotube protrusions from vesicles. In the present work, we report the unique case of topologically-connected nanotubes-vesicles obtained in the absence of directional forces, in single-component membranes, composed of an anisotropic bolaform glucolipid, above its melting temperature, T_m. Cryo-TEM and fluorescence confocal microscopy show the interconnection between vesicles and nanotubes in a single-phase region, between 60° and 90°C under diluted conditions. Solid-state NMR, necessarily recorded on the dry powder, yet demonstrates that the glucolipid can simultaneously assume two distinct configurations, head-head and head-tail. These arrangements, seemingly of comparable energy above the T_m, could explain the existence and stability of the topologically-connected vesicles and nanotubes, which are generally not observed for classical single-component phospholipid-based membranes above their T_m.

Keywords: *Nanotube vesicle networks; Tunnelling nanotubes*; *Block liposomes; Liposomes; Lipid nanotubes; Biosurfactants; Microbial glycolipids;*

Introduction

Topological connections between closed lipidic compartments through nanotubes[1–3] have been shown to play a crucial role in the transfer of matter and communication in neighboring mammalian cells.[4] These singular nanosystems, observed since the ‘90s as spontaneous non-equilibrium structures in electroformed model liposome membranes,[5,6] have since been largely studied, both experimentally and theoretically.[7–9] Addressed in the literature by different terms, tunnelling nanotubes (TNT),[1,4,9] block liposomes[10–12] or nanotube-vesicle networks,[13–16] (instead of tubes, some work speak of tethers[6,17]) all refer to a similar phenomenon, driven by various internal or external forces. The latter must overcome the energy barrier needed to bend a phospholipid bilayer from low positive mean and gaussian curvatures (vesicle) to a high mean and zero Gaussian (tube) curvatures.

A large body of both experimental and theoretical work has shown that budding and eventual nanotube formation from an existing membrane can only occur spontaneously for membranes of at least two-components[9,10,24,25,11,12,18–23] and below a vesicle-nanotube phase transition event.[26,27] Otherwise, external anisotropic driving forces like electroformation,[5–8,28,29] osmotic pressure,[6] laser "tweezers"[30] or electrodynamics[13–16] must be employed to obtain similar results with, in some cases, an impressive degree of 2D and 3D organization.[13–16] The origin of spontaneous nanotube formation has been shown to be related to a nanoscale phase separation between two membrane components, stabilizing low and high curvatures respectively,[10–12,31] with at least one component being highly anisotropic.[20,32,33] Theoretically, this behavior has been explained by deviations in the elastic properties of membranes due to in-plane orientational ordering of membrane inclusions composed of anisotropic amphiphiles, these referring to a non-symmetrical shape upon a 90° tilt along the amphiphile axis.[8,9,19,24,25,33]

In this work, we show unexpected nanotubing of membranes prepared from a single-component lipid, in the absence of external directional forces and above the lipid's T_m. This phenomenon is observed for a novel anisotropic double amphiphile (bolaform amphiphile, or bolaamphiphile), a glucolipid composed of β-D-glucose and a C18:1-*cis* fatty alcohol (G-C18:1-OH, Figure 1). This compound is obtained by microbial fermentation of a genetically-modified *S. bombicola* yeast in the presence of oleyl alcohol[34] and is developed in the broader context of extending the library of new biobased surfactants and lipids, in view of replacing petrochemical low molecular weight amphiphiles.[35–41] The structure of G-C18:1-OH is analogous to that of other microbial glycolipids developed through genetic engineering.[42,43]

Topological connections between nanotubes and vesicles are observed by means of cryogenic transmission electron microscopy (cryo-TEM), fluorescence microscopy and wide angle X-ray scattering (WAXS) above the melting temperatures, T_m= 48.3°C under strong dilution (0.5 wt%). Spin diffusion and ^{1}H double-quantum single-quantum (DQ-SQ) 2D solid-state nuclear magnetic resonance (ssNMR) spectroscopy under magic angle spinning (MAS), necessarily performed on the dry glucolipid powder, provides a spectroscopic ground to understand the vesicle-nanotube coexistence. The bolaform glucolipids could be in a head-head/tail-tail configuration in the vesicles, but rather in a head-tail configuration in the nanotubes. In the dry glucolipid, both configurations are energetically comparable in the single-phase region above T_m and their coexistence is evidenced by the splitting of some ^{13}C NMR signals. These facts could explain the stability of nanotubes, while the following hypotheses are formulated for their formation: membrane inclusions with different orientational ordering[13–16] possibly driven by inter-vesicle collisions.

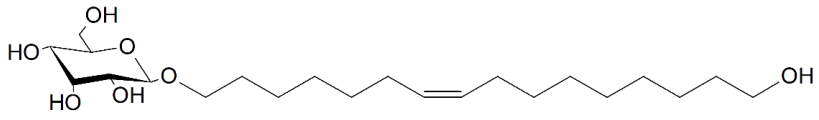

Figure 1 – Non acetylated C18:1 alcohol glucoside, G-C18:1-OH, is obtained by a bioprocess performed with modified *S. bombicola* yeast.

Experimental Section

Synthesis of non acetylated C18:1 Alcohol Glucosides (G-C18:1-OH). G-C18:1-OH (Mw= 418.56 g.mol^{-1}) was produced by aerobic whole cell bioprocess with a modified *S. bombicola* strain as described by Van Renterghem et al. (Fig. S4 in Ref. [34]). The molecule was purchased from the Bio Base Europe Pilot Plant (Gent, Belgium) and has the generalized chemical structure given in figure Figure 1. The HPLC and ^{1}H NMR spectrum (MeOD-d4) with peak assignment are shown in Figure S 1. High purity levels (99%) and high degree of uniformity were obtained, as can be derived from HPLC-ELSD chromatogram, ^{1}H NMR and table of contaminant given in Figure S 1.

^{1}H solution Nuclear Magnetic Resonance (NMR). ^{1}H solution NMR experiments were performed on a Bruker Avance III 300 spectrometer using a 5 mm ^{1}H-X BBFO probe using methanol-d4 as solvent. The number of transients is 8 with 3 s recycling delay, an acquisition time of 5.46 s and a receiver gain of 362. The ^{1}H NMR spectrum and relative assignment are shown in Figure S 1 and Table S 1. ^{13}C solution NMR were performed on the same probe using DMSO-d6. Corresponding chemical shifts are given in Table 1. Referencing is done with respect to TMS. δ_{1H}= 0 ppm, δ_{13C}= 0 ppm.

Sample preparation. The sample was dissolved in milliQ-grade water at the concentration of 5 mg/mL (0.5 wt%). Lack of pH-sensitive probes (e.g., COOH groups) in G-C18:1-OH, as otherwise found in other microbial amphiphiles,[44] but also the will to avoid ion-specific effects,[45] exclude the use of buffer. The solution was heat at the given temperature using a CH3-150 Combitherm-2 dry block heating device. For the cryo-TEM experiments, the vials were heat at the given temperature next to the cryofixation device and plunged into liquid ethane as fast as possible. For temperatures of 25°C and 70°C, the sample was heat at 90°C and then

cooled at to the desired temperature. For the SAXS experiment, the sample was heat at 90°C in the block heating device and cooled at to 25°C before analysis. For the SANS experiment, the sample was heat at 90°C directly in front of the beam using the thermalized sample holder available.

Differential Scanning Calorimetry (DSC). DSC was performed using a DSC Q20 apparatus from TA Instruments equipped with the Advantage for Q Series Version acquisition software (v5.4.0). Acquisition was performed on both hydrated and dry powder sample (~ 3-5 mg) sealed in a classical aluminium cup and using an immediate sequence of heating and cooling ramps at a rate of 10°C.min^{-1}. Melting temperatures, T_m, 1 and 2, T_{m1} and T_{m2}, were taken at the minimum of the endothermic peak.

Small and Wide Angle Scattering experiments. Small angle neutron scattering (SANS) experiments were performed at the D11 beamline of Institut Laue Langevin (Grenoble, France) during the run No. 9-13-778. Four q-ranges have been explored and merged using the following wavelengths, λ, and sample-to-detector (StD) distances. 1) ultra-low q: λ= 13.5Å, StD= 39 m; 2) low-q: λ= 5.3Å, StD= 39 m; 3) mid-q: λ= 5.3Å, StD= 8 m; 4) high-q: λ= 5.3Å, StD= 1.4 m. The sample (C= 5 mg.mL^{-1}) was prepared in 99.9% D_2O to limit the incoherent background scattering. The sample solution was analyzed in standard 1 mm quartz cells. Direct beam, empty quartz cell, H_2O (incoherent scatterer) within the quartz cell were recorded and boron carbide (B4C) was used as neutron absorber. The sample acquisition was measured at 90°C, where temperature was controlled through the controller thermalized sample holder available at the beamline. The background sample (D_2O) signal was subtracted from the experimental data. Absolute values of the scattering intensity were obtained from the direct determination of the number of neutrons in the incident beam and the detector cell solid angle. The 2D raw data were corrected for the ambient background and empty cell scattering and normalized to yield an absolute scale (cross section per unit volume) by the neutron flux on the samples. The data were then circularly averaged to yield the 1D intensity distribution, I(q). The software package Grasp (developed at ILL and available free of charge) was used to integrate the data, while the software package SAXSUtilities (developed at ESRF and available free of charge) was used to merge the data acquired at all configurations and subtract the background.

Wide-angle X-ray scattering (WAXS) was performed under temperature control at the SWING beamline of SOLEIL synchrotron facility (Saint-Aubin, France) during the run 20201747 (energy: 14 keV, sample-to-detector distance: 0.5 m). Two sample concentrations in

H_2O were probed, C= 5 mg.mL^{-1} and C= 25 mg.mL^{-1}. The 2D data were integrated azimuthally at the beamline using the software Foxtrot and in order to obtain the *I(q) vs. q* spectrum after masking the beam stop shadow. Silver behenate ($d_{(100)}$ = 58.38 Å) was used as a standard to calibrate the q-scale. Sample solutions were inserted in borosilicate capillaries of 1.5 mm in diameter. Capillaries were flame-sealed. A capillary oven with controlled temperature (± 0.5°C), provided at the beamline, was used to control the sample temperature between 25°C and 111°C. Data were normalized by the transmission and calibrated to the SAXS signal of H_2O at large q-values (I= 0.0163 cm^{-1}) in order to obtain an absolute intensity scale. The water signal was measured by subtracting the signal of the empty capillary from the signal of a water-filled capillary. The signal of (water + capillary) was used as background for the samples and it was subtracted after integration of the 2D data.

Cryogenic transmission electron microscopy (cryo-TEM). Cryo-TEM experiments were carried out on an FEI Tecnai 120 twin microscope operating at 120 kV and equipped with a Gatan Orius CCD numeric camera. The sample holder was a Gatan Cryoholder (Gatan 626DH, Gatan). Digital Micrograph software was used for image acquisition. Cryofixation was performed using a homemade cryofixation device. The solutions were deposited on a glow-discharged holey carbon coated TEM copper grid (Quantifoil R2/2, Germany). Excess solution was removed and the grid was immediately plunged into liquid ethane at -180°C before transferring them into liquid nitrogen. All grids were kept at liquid nitrogen temperature throughout all experimentation. Cryo-TEM images have been treated and analyzed using Fiji (is just ImageJ) software, available free of charge at the developer's website.[46]

The sample's concentration was C= 5 mg.mL^{-1}. For technical reasons, the temperature during cryofixation could not be controlled. For this reason, the temperature associated with each cryo-TEM image in the text was related to the equilibration temperature just before cryofixation, the device being as close as possible to the dry bath used for temperature control. Since temperature control during cryofixation was not possible in our device, and practically impossible at high temperatures, one should take the *T** values as indicative of the given value. Although the sample transfer between the dry bath and the cryofixation device was performed as fast as possible, it is more than likely that the actual temperature of the sample at the moment of cryofixation was lower than the one indicated here, although impossible to know precisely.

Fluorescence microscopy. Images were recorded using a 40x objective on a Leica SP5 upright confocal microscope with 405 nm laser excitation. The sample was marked with 6-dodecanoyl-N,N-dimethyl-2-naphthylamine (Laurdan, Mw= 353.54 g.mol^{-1}) fluorophore as follows. A stock solution of 3 mg of Laurdan in 100 µL of acetone was initially prepared (C= 30 mg.mL^{-1}). A volume of 0.28 µL of the stock Laurdan solution was diluted in 1 mL of a 5 mg.mL^{-1} G-C18:1-OH water solution temporary set at 110°C in a sealed Eppendorf. The latter was important so to enhance inclusion of Laurdan in the membrane constituted by the glucolipid, while in its vesicle phase. The final Laurdan concentration was approximately 24 µmol, with a molar Laurdan-to-G-C18:1-OH molar ratio of approximately 1-to-500. Fluorophore-to-lipid ratios above 1:200 were generally considered as non-interfering with the lipid phase behavior, as also verified in this work.

Laurdan can be excited between 365 nm and 410 nm and its emission wavelength can vary according to the rigidity of the membrane: intercalation within a rigid or flexible membrane generates emissions at 440 nm or 490 nm, respectively.[47] In the present experiment, we have flame-sealed a solution of G-C18:1-OH at 5 mg.mL^{-1} containing Laurdan (1-to-500 in lipid-to-Laurdan ratio) in flat optical capillaries of 0.1 mm thickness. Capillaries were set on a Linkam support for temperature control, eventually placed under the microscope. The sample was excited at 405 nm and detection was made in spectral mode with a 5 nm window sliding every 5 nm from 412 nm to 602 nm in 16 bits, which allows quantify the signal and compare the different conditions. Quantitative analysis was performed according to the literature:[48,49] several ROI (range of interest) have been drawn on several images using the ROI manager of Fiji (is just ImageJ) software. The integrated intensity of each ROI at 440 nm and 490 nm was eventually recorded and used to calculate the value of the generalized polarization, GP, as follows of

$$GP = \frac{(\lambda_{440} - \lambda_{490})}{\lambda_{440} + \lambda_{490}}$$

A negative GP indicates a flexible membrane while a positive GP indicates a rigid membrane.

Solid-state Nuclear Magnetic Resonance (ssNMR): ^{1}H and ^{13}C ssNMR experiments have been performed using an Avance III HD Bruker 7.05 T (ν_{1H}= 300 MHz) spectrometer and a 4 mm magic angle spinning (MAS) probe, except for the BAck-to-BAck (BABA) experiment, which was performed on an Avance III Bruker 16.44 T (ν_{1H}= 700 MHz) spectrometer equipped with 2.5 mm MAS probe. Temperature was controlled through a Smart cooler BCUII/a BCU-xtreme unit, using 10 min of equilibration time after each temperature variation. Temperature was

always varied from high (110°C) to low (70°C) before analysis. Due to combined use of fast MAS rates, necessary to achieve high resolution spectra, and heating close to the boiling point of water, neither diluted nor concentrated samples could be used for ssNMR experiments. All tests employing up to 50 wt% G-C18:1-OH in water resulted in sample centrifugation, drying but also expulsion from the rotor, causing sudden stop of rotor spinning. For these reasons, all attempts to study hydrated G-C18:1-OH failed and only the dry powder could be analyzed. The dry sample powder was analyzed as such in zirconia rotors (4 mm or 2.5 mm) spinning at MAS= 10 kHz (4 mm) or 22 kHz (2.5 mm). and Chemical shifts were calibrated with respect to adamantane (^{13}C: δ_{13C}(CH2)= 38.48 ppm; δ_{1H}= 1.91 ppm) and glycine alpha (δ_{13C}(CO)= 176.03 ppm). Details on the acquisition parameters are given in the Supporting Information.

Results and discussion

Topologically-connected nanotubes and vesicles

G-C18:1-OH is a biobased glucolipid, water-insoluble at room temperature, and of which the physicochemical properties are poorly known. The DSC thermogram performed at 10°C/min of G-C18:1-OH as a function of the water content (Figure 2a) shows two endothermic peaks on the dry powder (99.6 wt% glucolipid). They are attributed to two melting phenomena occurring at the following temperatures, T_m: 48.3°C (T_{m1}) and 95.7°C (T_{m2}), the enthalpy of the former being lower than that of the latter. Interestingly, DSC also shows that T_{m1} is hydration independent and reversible (the associated exothermic peak is systematically observed), while the transition at T_{m2} is simply suppressed (here tested up to 130°C) on hydrated powders and never observed on the cooling profile, even at slow cooling rates (1°C/min). The thermogram recorded on the dry powder is typical of single-component lipids having an intermediate,[50] metastable, phase (often referred to the ripple phase, $P_{\beta'}$, in reference to the periodic undulation of the bilayer),[50–54] between the classical lamellar gel (L_β) and liquid crystalline (L_α) phases[50–54] and characterized by regions of both liquid order and disorder.[54,55] The effect of water does not influence the low-temperature crystallization at T_{m1}, but it contributes to disrupt the ordered array of hydrocarbon chains in the metastable phase.

On the basis of the DSC thermogram, the aqueous phase behavior of G-C18:1-OH under diluted conditions (5 mg.mL^{-1}) was studied at four different temperatures (red marks on Figure 2a): below and above T_{m1}, but also between T_{m1} and T_{m2}, corresponding to the thermogram of the dry powder.

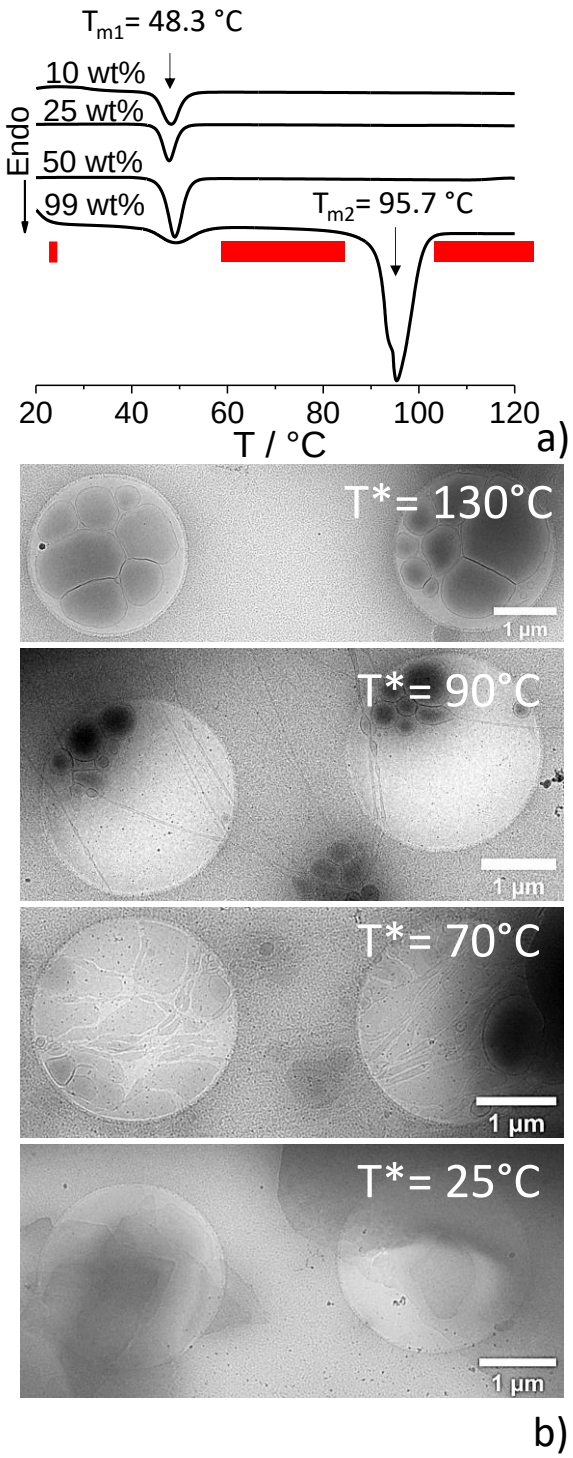

Figure 2 – a) DSC thermogram of G-C18:1-OH under dry (0.4 wt% water, estimated by thermogravimetric analysis) and hydrated conditions recorded at a heating rate of 10°C/min. Red marks indicate the temperatures at which cryo-TEM experiments are performed on the corresponding 5 mg/mL aqueous solutions. b) Cryo-TEM images recorded for a 5 mg/mL G-C18:1-OH aqueous solution heat at *T= 130°C, 90°C, 70°C and 25°C. *T** indicates the temperature of the sample solution before cryofixation. *T**≠ T, T being the temperature of the sample upon plunging in liquid ethane. Please refer to the materials and methods section for more information.**

The series of cryo-TEM images in Figure 2b show an overview of the most relevant structures observed on G-C18:1-OH solution from T^*= 130°C to T^*= 25°C, whereas T^* is indicative of the equilibrium temperature before cryofixation (refer to materials and methods section for more information on the sense and interpretation of T^*). At T^*> 100°C, the sample is essentially composed of polydisperse single wall vesicles, massively shown by the complementary pictures presented in Figure S 2. In between T_{m1} and T_{m2}, at T^*= 90°C and T^*= 70°C (Figure 2b, Figure 3, Figure 4, complemented by Figure S 3 and Figure S 4), vesicles are connected by nanotubes. At T^*< T_{m1}, flat crystals are otherwise observed (Figure 2b and Figure S 5).

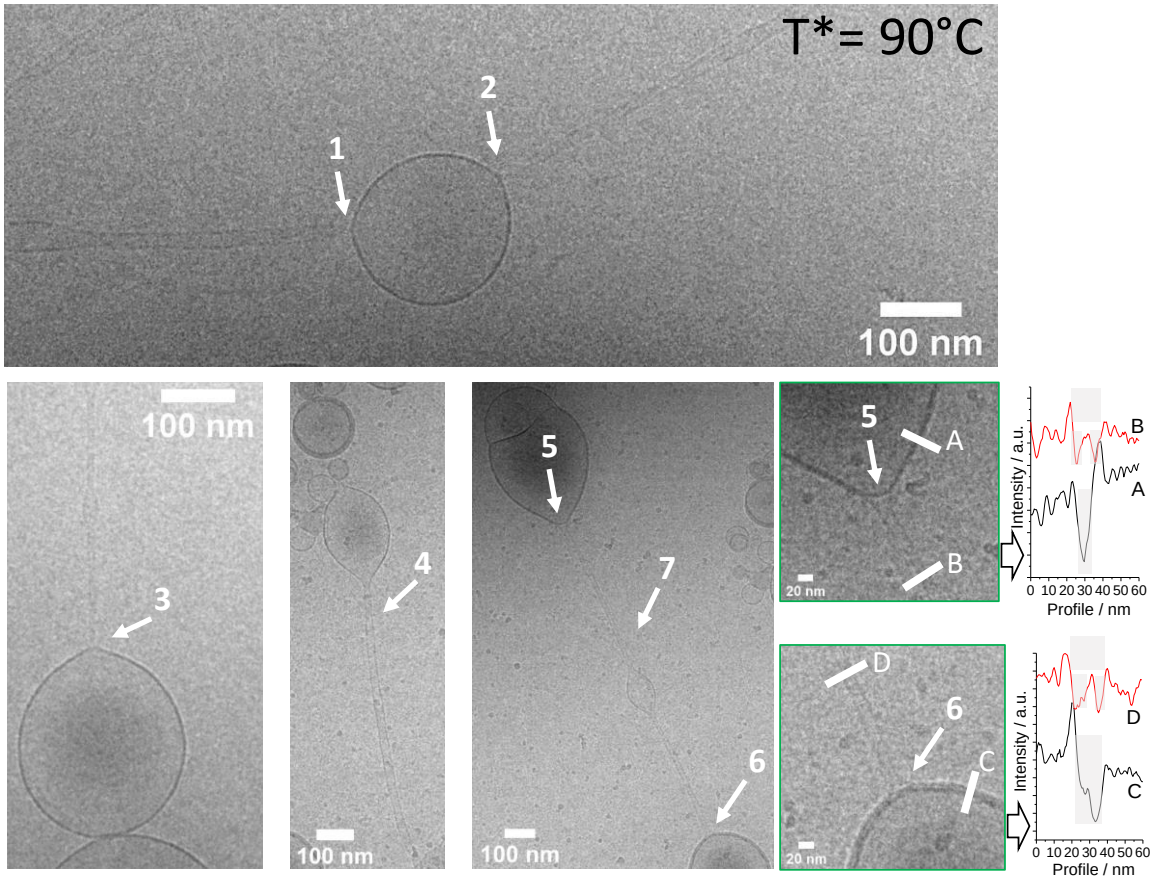

Figure 3 – Cryo-TEM images recorded for a 5 mg/mL G-C18:1-OH aqueous solution heat at T^*= 90°C.

A deeper insight at T^*= 90°C is given in Figure 3 (more images are provided in Figure S 3). Arrows 1 through 6 mark very clearly the typical continuity in the glucolipid membrane between the vesicle and nanotubes. Arrow N° 7 shows that a single nanotube connects the outer membrane of two vesicles several hundred nanometers apart. The connection is shown by

arrows N°5 and N°6. The corresponding profiles, A through D, confirm the tubular nature of the elongated objects. Profiles B and D are both characterized by typical symmetrical thick walls (low intensity depths highlighted by shaded rectangles) surrounding a hollow region (high intensity peak, between the shaded rectangles). The wall thickness varies between 3.5 and 4.0 nm for profile B and between 4.1 and 6.1 nm for profile D, while the total nanotube diameter varies between 14 nm at B and 20 nm at D. At the same time, the thickness of the vesicle wall is about 6 nm at A and 13.5 nm at C. Considerations about the bilayer or interdigitated structure of the membrane will be presented below.

The connection between nanotubes and vesicles seems to be multiple. For instance, arrow N°1 (Figure S 3) and N°4 (Figure 3) show a single-wall vesicle, of which the membrane is extruded into a nanotube. Similarly, a closer look at arrows N°1, 2 and 3 in Figure 3 show that the vesicle is single-wall and fully closed, while the nanotube nucleates at the vesicle outer surface, with no apparent topological continuity. In many regions of the sample at T^*= 90°C, one can find exvaginations or buds[23,25,31] in the nanotube wall. This is shown, for instance, by arrows N°7 and particularly put in evidence in Figure 4 by arrows N°1 through N°4, where the amplitude of the oscillation varies between 20-25 nm (arrow N°1) and 6-8 nm (arrows N°3-4).

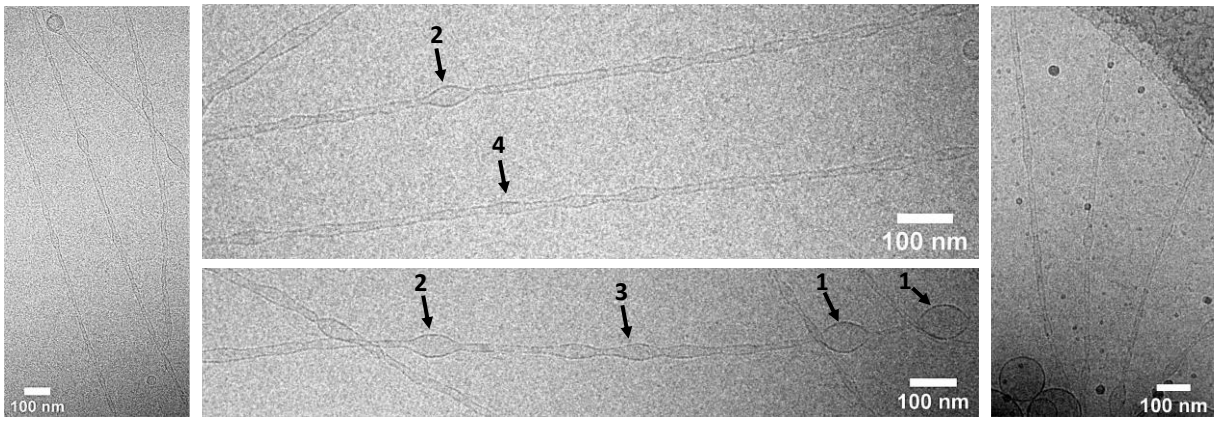

Figure 4 - Cryo-TEM images recorded for a 5 mg/mL G-C18:1-OH aqueous solution heated at T^*= 90°C.

Still between T_{m2} and T_{m1}, but at lower temperature (T^*= 70°C), the nanotubes seem to vary from single threads (arrow N°1, Figure S 4) to nanotubes of diameter below 15 nm, both connecting nanotubes of diameter ranging between 50 nm and 100 nm (arrows N°2, Figure S 4). The larger tubes are most likely formed by the inflation and flattening of the nanotubes, probably after assimilation of surrounding vesicles and fusion of the exvagination discussed above. The transition between vesicles, tubes and flat membranes is certainly more accentuated. Arrow N°3 in Figure S 4 shows distinct vesicles while arrow N°4 identifies a flat structure evidently formed from fused vesicles. In particular, arrow N°5 points at the fusion of two

vesicles while arrow N°6 points at two vesicles fusing into the flat membrane. Additional areas where vesicle fusion is prominent are indicated by the oscillations at the outer skirt of broad lamellae and pointed by arrow N°7.

Finally, below T_{m1}, at T^*= 25°C for instance, mainly flat crystals, with no visible exvaginations or tubes, are visible (Figure S 5) by cryo-TEM and the material turns into an insoluble precipitate. Massive presence of flat crystalline structures is also clear from the bulk iridescent behavior of a G-C18:1-OH solution under manual shear.

In summary, despite the uncertainty related to the actual state of equilibrium of the glucolipids at the moment of cryofixation, cryo-TEM depicts a vesicle phase at T> 100°C, a flat lamellar phase below T_{m1} and an interconnected vesicle-nanotube network between T_{m1} and about 100°C. The combination of statistically-relevant fluorescence microscopy and scattering/diffraction experiments provides an additional proof of the coexistence of vesicle/nanotube systems between the two transition temperatures. Please note that the experiments reported below have been performed under controlled conditions of temperature, which is then indicated by the use of T, instead of T^*.

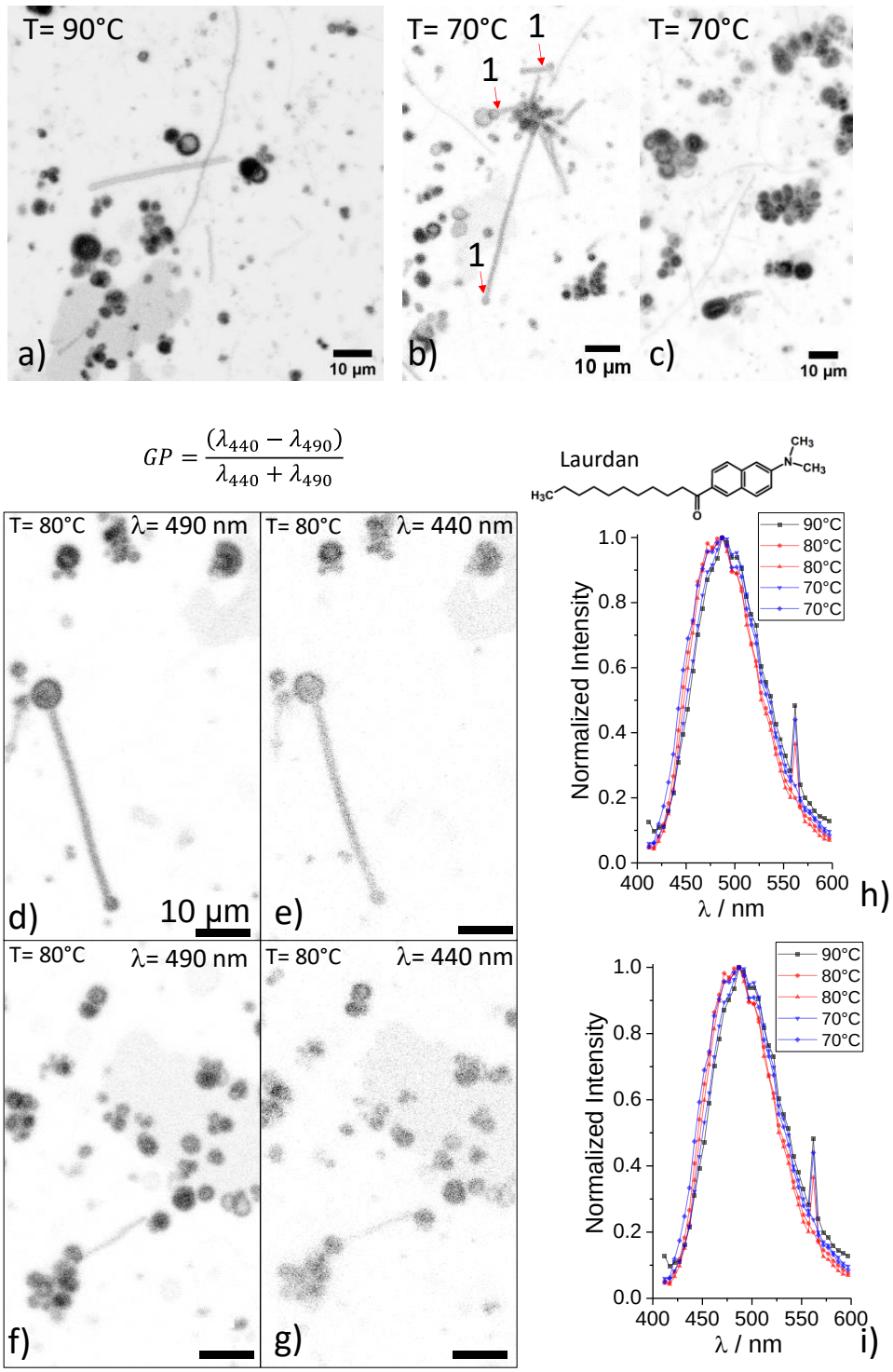

Figure 5 – a-c) Confocal fluorescence microscopy images recorded at 90°C and 70°C for a 5 mg/mL G-C18:1-OH aqueous solution. d-g) Typical fluorescence microscopy images recorded at T= 80°C using Laurdan (refer to materials and methods section for more details on this fluorophore). Excitation wavelength is 405 nm for all the images, while emission wavelength is 490 nm in (d,f) and 440 nm in (e,g). h) Full emission spectra obtained from the integration of various fluorescence images recorded from 412 nm to 600 nm (step: 5 nm) at 90°C, 80°C and 70°C. i) Box plot of GP, defined as $GP = \frac{(\lambda_{440} - \lambda_{490})}{\lambda_{440} + \lambda_{490}}$ with λ_{440} and λ_{490} being the emission wavelengths at 440 nm and 490 nm, at 90°C, 80°C and 70°C. Each data point

corresponds to a set of regions of interest (ROIs) (54 at 90°C, 65 at 80°C and 75 at 70°C) selected in the corresponding fluorescence images. ROIs were representatively selected so to include the entire image but also vesicles alone, tubes alone and mixtures of vesicles and tubes.

Figure 5a,b shows two typical confocal fluorescence microscopy images recorded on a G-C18:1-OH solution (5 mg/mL) in a flame-sealed capillary heat at T= 90°C and T= 70°C. Although the resolution of optical microscopy is not comparable with cryo-TEM, the sample is broadly composed of vesicles coexisting with nanotubes, whereas in some cases the nanotube starts from the vesicle itself (arrow N°1), in good agreement with cryo-TEM data. Furthermore, SANS recorded at T= 90°C (Figure S 6a) shows a scattering profile with a pronounced -2 dependence of the scattering intensity against the wavevector q in the log-log scale. This indicates the massive presence of a flat interface and it is expected typical of bilayers in vesicular morphologies.[56] However, the typical signature of nanotubes cannot be observed in the SANS profile, and this can be explained by both an argument related to the relative lower amount of nanotubes with respect to vesicles at 90°C but also to the steeper slope of flat morphologies (-2) compared to tubes (-1), the signal of the former masking the tube signal at low wavevector values. The SANS profile is characterized by a diffraction peak at q= 0.167 $Å^{-1}$, of which the assignment is refined by WAXS data.

Temperature-driven WAXS experiments in Figure S 6b,c (5 $mg.mL^{-1}$ and 25 $mg.mL^{-1}$, respectively) show a lamellar order, possibly attributed to a multilamellar structure of the vesicles (d_v, Figure S 6d) at high temperature and to the interplanar arrangement of the crystalline flat structures (d_L, Figure S 6d) at T= 25°C. The sharp (001) reflection indicates typical interlamellar distance of 35.3 Å at 25°C, although this value varies with temperature (40.0 Å at 111°C, 37.2 Å at 88°C), thus confirming its assignment to a hydration-dependent interlamellar order. More intriguing is the second, broader, peak at q= 0.403 $Å^{-1}$ (d= 15.6 Å) and its reflection, both clearly visible at 88°C, below T_{m2}. We attribute it to the inter-glucolipid arrangement inside the tubular phase (d_t, Figure S 6d), coexisting with the vesicle phase, between T_{m1} and T_{m2} and to the planar lipid arrangement (d_i, Figure S 6d) in the rigid flat lamellar structure, below T_{m2}. Its temperature-, hence hydration-, independent position also confirms its structural origin. Finally, besides the water-structure peak at about 2 $Å^{-1}$, we also observe a broad peak at 1.44 $Å^{-1}$, characteristics of the lateral packing (d*, Figure S 6d) of lipids in bilayers. While its position could be consistent with an L_α phase[57,58] above T_{m2}, its broadness and positional invariance as well as the coexistence between vesicles and tubes do not allow a precise assignment.

Does G-C18:1-OH assume a bilayer or interdigitated structure, the latter being the one found for other similar bolaform glucolipids?[42,43] The size of G-C18:1-OH can be estimated to be at the most 32 Å, given by the length, L, of the C16 tail (L = 22 Å, from the Tanford formula, L= 1.54 + 1.265 × n, (n= 16)[59]) and the sugar (about 10 Å).[42,43] However, the *cis* conformation of the C=C bond imposes a "kink" of 60° in the aliphatic chain, which reduces the effective length of the oleic backbone to about 17 Å, for an effective total G-C18:1-OH length of about 27 Å. Cryo-TEM provides a tube thickness varying from 35 Å to 60 Å and a vesicle membrane thickness of at least 60 Å. WAXS suggests an interlamellar thickness (membrane and water) between 40 Å and 37 Å and an inter-lipid distance in the tube of about 16 Å. In the absence of a clear form factor oscillation profile, as found for similar glucolipids,[42,43] one must acknowledge that these data pledge neither in favor of fully interdigitated nor a double layer structure and might suggest a tilted lipid arrangement with partial interdigitation.[60]

^{13}C ssNMR demonstrates that G-C18:1-OH can assume two coexisting, head-head and head-tail, configurations

Vesicles are characterized by low positive mean and gaussian curvatures, while nanotubes are described by a combination of a high positive mean and zero gaussian curvatures. In this regard, the coexistence of vesicles and nanotubes requires glucolipids to adapt themselves to both environments at the same time. For this reason, the formation of nanotube-vesicle networks generally requires a specific driving force, able to impose a high mean and zero gaussian curvature to the membrane. In many systems, insertion of at least a second constituent (lipid, surfactant, protein) in the membrane becomes a necessary internal driving force for the nucleation and growth of so-called membrane inclusions, from which topologically-connected nanotubes can form,[10–12,32,61] as explained by orientational ordering arguments.[62] It has also been shown that external driving forces, such as use of laser "tweezers",[30] osmotic pressure,[6] electroformation[5–8,28,29] or controlled suction,[13–16] are otherwise necessary, as also supported by theoretical studies.[19]

The bending energy of tubes is higher than that of a vesicle membrane,[8] due to the dependence of the membrane free energy from the principal curvatures. For this reason, isotropic (rotational symmetry along the main axis), but also anisotropic,[33] lipids generally stabilize low-curvature shapes, like flat membranes or vesicles. Lipid nanotubes are also a common phase formed by amphiphiles, but generally for lipids with a certain complexity in their molecular structures, as exampled by diacetylenic derivatives of phospholipids, among others.[26,27,63–65] Negative contributions to the bending energy favoring the simultaneous

presence of interconnected vesicles and tubes was shown to be driven by the presence of anisotropic lipids in a membrane continuum. Spontaneous deviations to the elastic theory in the presence of surfactants, lipids and proteins with anisotropic structures favor the formation of protrusions with radius of the order of the fraction of a micron.[9–12,19–23,62]

In the absence of both internal and external driving forces mentioned above, G-C18:1-OH should behave as a standard lipid. Its DSC profile (Figure 2)[53,66,67] under both hydrated and dry conditions identifies a hydration-independent transition (T_{m1}) slightly above room temperature; this is followed by one main transition at higher temperature (T_{m2}) in the dry sample.[50] For such a profile, one expects a gel phase (L_β) below T_{m1} and a liquid crystalline structure, possibly in the morphology of vesicles (L_4 phase), possibly above $T_{m1,}$ and most likely above T_{m2},[31] as experimentally found. On the basis of the thermogram recorded on the dry powder, one may also expect a "ripple" (P_β) phase between T_{m1} and T_{m2} characterized by periodic undulations of the bilayer (generally addressed to as regions with both liquid order and disorder).[54,55]

In the present work, instead of a L_β phase, we observe flat crystals below T_{m1}, and a vesicle-nanotube network instead of the "ripple" phase. The latter is particularly unexpected because the membrane is composed of a single-component (G-C18:1-OH) and no anisotropic external force (osmotic, hydrodynamic, electric) is used to pull and stabilize the tubes. In addition, the nanotubes are observed at fairly high temperatures, above T_{m1} (between about 60°C and 90°C), while this morphology is generally favored at low temperature (proportionality with 1/kT, figure 5 in Ref. [62]), commonly below a given transition temperature, characteristics for each specific amphiphile.[27] Furthermore, nanotubes of G-C18:1-OH seem to be stable in time, thus differing from what is found in electroformed vesicles.[7,8] They are also observed away from phase transition events (may them be at T_{m1} or T_{m2}), as otherwise reported before for a diacetylenic derivative of phosphatidylcholine[26] and many other systems.[27]

A stable nanotube-vesicle network for a single-component phospholipid in the absence of external driving forces is not expected and has never been reported before. It could be explained by the coexistence of two micro-separated phases of different rigidity. This hypothesis is excluded by confocal microscopy on Laurdan-labelled membranes and magic angle spinning (MAS) solid-state NMR (ssNMR) experiments.

Laurdan is a well-known fluorophore used to put in evidence the coexistence of rigid and fluid domains in both model and biological membranes.[47–49] Laurdan was used here to label the G-C18:1-OH membranes between T_{m1} and T_{m2} and to verify the possible micro-segregation and coexistence of rigid (e.g., L_β, λ_{em}= 440 nm) and fluid (e.g., L_α, λ_{em}= 490 nm) domains, in

tubes and vesicles, respectively. A set of quantitative experiments performed on a 5 $mg.mL^{-1}$ solution, summarized in Figure 5, shows an excess of fluorescence at only λ_{em}= 490 nm for temperature between 90°C and 70°C (Figure 5h). The GP value, which quantifies the rigid/fluid character of the membrane, is systematically negative (Figure 5i), indicating an overall fluid membrane at all temperatures. GP is quantified on more than 50 regions of interest (ROIs) at each temperature, including vesicles and tubes alone as well as connected nanotube-vesicles (Figure 5d-g). The dispersion of GP at 80°C and 70°C between -0.8 and -0.2 could suggest the spurious presence of membranes with various degrees of flexibility, although fluidity is always predominant. The combination of WAXS (broad peak, d*= 1.44 $Å^{-1}$, invariant with temperature, Figure S 6b,c) and confocal fluorescence microscopy using Laurdan confirms the single-phase of the membrane composed of G-C18:1-OH, both in vesicles and nanotubes. This is also consistent with the lack of phase transitions in DSC experiments between ~85°C and ~60°C, especially in hydrated samples. We conclude that the vesicle-nanotube transition is not driven by the local segregation of gel phase (L_β) microdomains, nor that the nanotubes are composed of such phase.

ssNMR is the best-suited approach to investigate the origin of the local driving force for the nucleation of anisotropic inclusions, of which the average orientation depends on the local membrane and inclusion curvatures and was shown to promote tubing.[62] ssNMR can provide information on the local molecular mobility, e.g. through the nuclear spin relaxation behavior, but also on intermolecular interactions and stereochemistry, e.g. through variations in the chemical shift.[68–70]

Ideally, ssNMR should be performed on diluted G-C18:1-OH samples above T_{m1}. However, fast MAS, necessary for high resolution, centrifuges the sample. As a first approximation, hydrated G-C18:1-OH samples, for instance at 50 wt% as classically done for phospholipids,[71] could be studied. Unfortunately, permeability of the sample holder combined to heating (close to the boiling point of water) and MAS provoke dehydration and even sample ejection. After experiencing both of the above, this approach was abandoned. As a second approximation, the study of the dehydrated G-C18:1-OH powder avoids centrifugation and evaporation. If studying dried lipids may not reflect their exact behaviour under diluted conditions, valuable structural information can still be obtained in dehydrated molecular systems, like proteins, thus illustrating that this approach is not unreasonable. Furthermore, if DSC (Figure 2a) shows that hydration suppresses the T_{m2}, it also shows that the value of T_{m1} is not affected by water at concentrations as low as 10 wt%. For this reason, performing a structural analysis of dehydrated G-C18:1-OH by ssNMR above T_{m1} may help understanding

the local arrangement of G-C18:1-OH in two morphologies, vesicles and nanotubes, having sensibly different curvatures.

To explore the local mobility of the most relevant chemical groups of G-C18:1-OH above T_{m2} (T= 110°C) and between T_{m2} and T_{m1} (70 < T / °C < 90), we combine a series of ^{1}H and ^{13}C experiments. Single-pulse (SP) MAS experiments (^{1}H and ^{13}C), when recorded under quantitative conditions, allow the detection of all chemical species, while cross-polarization (CP) MAS (^{13}C only) experiments are sensitive only to constrained groups, for which the ^{1}H-^{13}C dipolar coupling is not averaged to zero by the molecular motions.

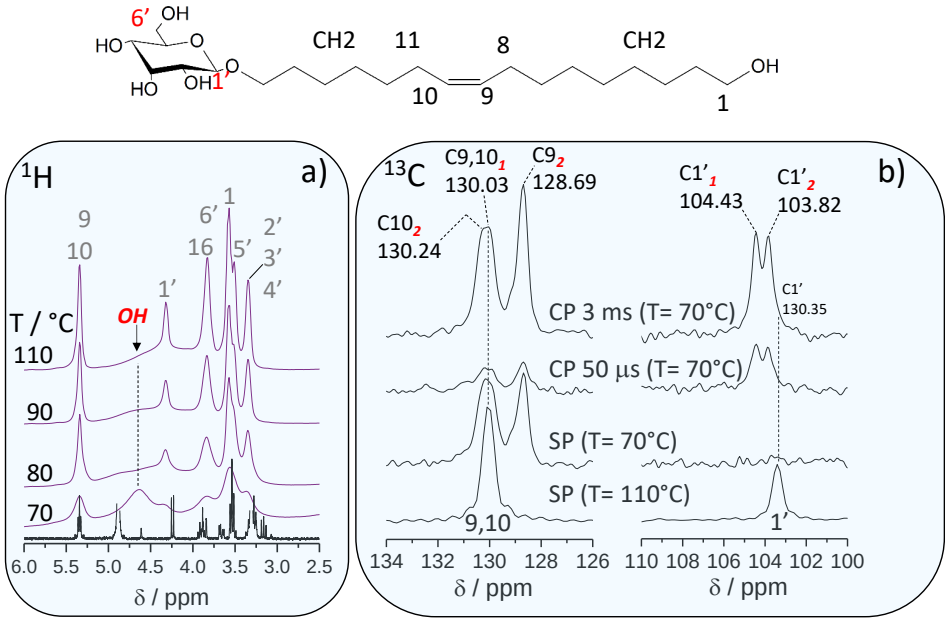

Figure 6 – a) ^{1}H MAS (10 kHz) ssNMR spectra recorded from 110°C to 70°C. b) ^{13}C MAS (10 kHz) ssNMR spectra recorded using high power decoupling single pulse (SP) and cross-polarization (CP) pulse sequences. Contact time for CP experiments and corresponding temperatures are given on each spectrum. Full spectra are given in Figure S 7.

The most relevant ^{1}H and ^{13}C spectra are given in Figure 6 (full range in Figure 7 and Figure S 7). As expected, the ^{1}H solid-state SP/MAS spectra show broader peaks compared to the solution-state NMR spectrum (Figure 6a), reflecting the obvious solid-state character of the sample at any temperature. The sugar group and the C=C bond resonate in the 2.5-6 ppm range and 5.35 ppm, respectively, while the OH groups of the sugar moiety are found below 4.5 ppm (Figure 6a, full assignment in Table S 1). Very broad (~1 ppm) at 100°C, the position of the OH peak varies with the temperature value and becomes narrower (<~0.5 ppm) and visible at δ_H= 4.64 ppm at T= 70°C. Line narrowing and chemical shift variations of the OH resonance in ssNMR is always a direct sign of H-bonding interactions, whereas the strength of the H-bonding, hence its OH···H distance, is correlated to a dispersion in chemical shifts.[72–75] All other

resonances broaden from 110°C to 70°C, thus indicating slower and/or more anisotropic reorientational motions of all chemical groups. The specific dynamic behaviour of the sugar headgroup is also reflected by its ^{1}H transverse relaxation time, T_2, whereas the shorter the T_2, the higher the rigidity. Experiments performed between 110°C and 70°C, shown and commented in Figure S 8 in the Supporting Information, globally show a single, short (< 1 ms below 100°C), T_2 relaxation component for H1', H5' and H6' and two, both short and long (between 4 ms and 12 ms) T_2 for the acyl chain ($C\underline{H}_2$, H9,10, H8,11), even below 100°C.

At 110°C, ^{13}C SP/MAS experiments (Figure 6b, full range in Figure 7 and Figure S 7, assignments in Table 1) show a single peak at δ_C= 103.35 ppm for C1' and at δ_C= 130.03 ppm for C9,10, as expected for a symmetrical conformation with two chemically-equivalent carbons.[76] At 70°C, the C1' peak disappears, while C9,10 now shows two peaks around 128 ppm and 130 ppm (Table 1; full temperature series in Figure S 7b), attributed to $C9_2$ (δ_C= 128.69 ppm) and C10 in a non-symmetric configuration respectively, for which these two carbons are chemically inequivalent.[76] More precisely, the resonance at 130 ppm is actually the superposition of two close resonances, $C9,10_1$ (δ_C= 130.03 ppm) and $C10_2$ (δ_C= 130.24 ppm), where subscripts 1 and 2 stand for two different conformations of the *cis*-olefin group, as reported for various phases of oleic acid in the vicinity of 0°C.[76]

Table 1 – ^{13}C Chemical shifts of G-C18:1-OH in solution and solid-state. Solid-state experiments are recorded at MAS= 10 kHz. All spectra are reported in Figure 7 and Figure S 7. The contact time for cross polarization is 3 ms. In all ssNMR experiments, temperature is first raised at 110°C and then lowered to either 90°C or 70°C. Attribution of the ^{13}C resonances in Table 1 is performed on the basis of the solution spectrum (Figure S 1b). Additional peaks observed in both single pulse and cross polarization ssNMR experiments are attributed, when possible, to a configuration effect of the given atom, e.g., $C9,10_1$ and $C9_2$ indicate two configurations of C9. All new peaks observed in solid-state and not detected in solution are highlighted in red for convenience.

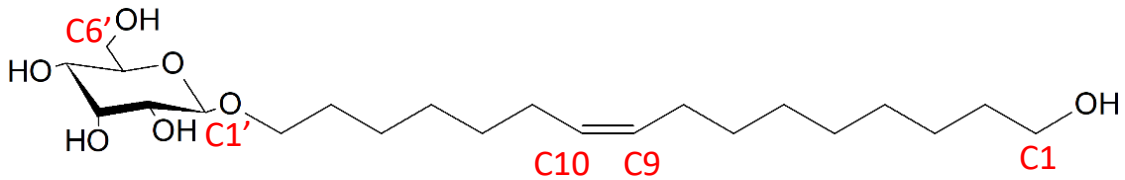

		δ / ppm			
Peak	Liquid (DMSO-d6)	Solid Single Pulse T= 110°C	Solid Single Pulse T= 90°C	Solid Single Pulse T= 70°C	Solid Cross Polarization T= 70°C
$C10_2$		-	-	130.24	130.24
$C9,10/C9,10_1$	130.09	130.03	130.03	130.03	130.03

C9$_2$	-	-	-	128.69	128.69
C1'/C1'$_1$	103.29	103.35	103.35	-	104.43
C1'$_2$	-	-	-	-	103.82
C3'	77.24	77.09	77.02	-	78.29
?	-	76.34	76.29	-	76.21
?					75.25
C2'	73.88	73.98	73.90	73.70	73.70
C4'	70.52	70.77	70.54	70.41	70.98
C16	69.00	70.16	-	-	70.29
?	-	-	-	-	67.93
C1,C5',C6'	61.53	62.41	62.36	62.39	62.62
C1,C5',C6'	61.17	-	-	-	59.56
C2'	33.00	32.90	32.90	32.83	32.79
CH2(*trans*)	-	-	-	31.98	31.96
CH2(*gauche*),C15	29.41	29.81	29.87	30.04	-
C8,11	27.06	27.47	27.47	28.32	28.17
CH2	25.97	26.25	26.28	26.30	28.17

^{13}C CP/MAS spectra at 70°C (Figure 6b, full range in Figure 7 and Figure S 7d) at increasing contact times confirm the presence of two *cis*-olefin environments: one for which C9,10 are equivalent, labelled here C9,10$_1$, and one for which they are inequivalent, labelled C9$_2$, C10$_2$. Both environments are rigid enough to be observed at short contact time (t_c= 50 µs). A similar double environment is also observed for the sugar C1': CP/MAS at 70°C shows two peaks (C1'$_1$ at δ_C= 104.43 ppm, C1'$_2$ at δ_C= 103.82 ppm, Figure 6b, Figure S 7d). These are significantly shifted downfield from the C1' peak observed at 110°C and are detected at contact times as short as 50 µs, thus indicating their rigid character. One also finds that CP/MAS is totally inefficient at 100°C for short contact times (50 µs) and poorly efficient even at 3 ms, typical of fast-tumbling molecules (Figure S 7c); also, both *gauche* (δ_C= 30.04 ppm) and all-*trans* (δ_C= 31.98 ppm) conformations of the CH_2 carbons coexist at 70°C (Figure S 7b).[77]

According to ssNMR, one main, mobile, molecular environment exists at 110°C, as shown by the well-resolved ^{1}H spectrum, single C=C (C9,10$_1$) and anomeric (C1') resonances, *gauche* conformation of the aliphatic CH_2 and single T_2 of the aliphatic CH_2 chain and sugar protons. The sugar group is certainly mobile (inefficient ^{1}H→^{13}C CP/MAS) but still more constrainted than the acyl chain (shorter T_2 (^{1}H)). As the temperature is lowered, the overall rigidity increases (broadening of ^{1}H NMR peaks, faster ^{1}H transverse relaxation and efficient ^{1}H→^{13}C magnetization transfer during CP/MAS), presumably driven by H-bonding interactions (downfield shift and line narrowing of the OH ^{1}H signal, very short OH T_2, loss of the C1' signal in SP/MAS). At the same time, a number of spectroscopic data (two concomitant

resonances for: anomeric C1'$_1$ and C1'$_2$, *cis*-olefin C9,10$_1$ and C9$_2$, C10$_2$, and CH_2, *gauche* and all-*trans*, environments) and relaxation behaviour (fast and slow T_2 relaxation components) strongly suggests the coexistence of two molecular environments. Further proofs of the coexistence of two distinct molecular domains are given by a number of chemical shift variations in the ^{13}C CP/MAS spectrum at 70°C compared to the one at 110°C, 90°C and solution. This is shown in Figure 7 and in the list of ^{13}C chemical shifts in Table 1.

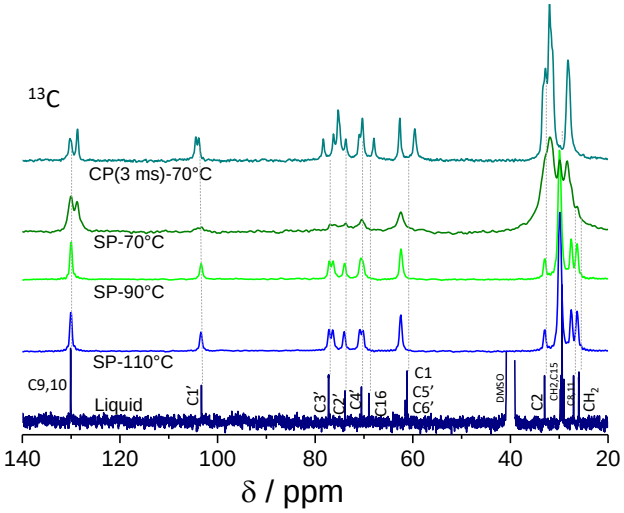

Figure 7 - Comparison between solution- and solid-state ^{13}C NMR spectra of G-C18:1-OH. Solid-state experiments are recorded directly on the sample powder at a MAS of 10 kHz (4 mm zirconia rotor). SP: Single Pulse; CP: Cross Polarization. In all the ssNMR experiments, temperature is first raised at 110°C and then lowered to either 90°C or 70°C. Segmented lines are meant to highlight the known peak position in solution, thus stressing the strong chemical shift variations in the solid-state.

NMR experiments above T_{m2} suggest that vesicles could contain G-C18:1-OH with a single family of mobile conformations, characterized by chemically-equivalent C=C (red, Figure 8b) and a single C1' conformation (green, Figure 8b). Experiments between T_{m1} and T_{m2} otherwise suggest that two coexisting conformations, characterized by chemically-equivalent (red, Figure 8b) and inequivalent (magenta, Figure 8b) C=C, could be associated to nanotubes. Two distinct C1' sites (grey, Figure 8b) also indicate two configurations of the sugar headgroup. A comment on this point will be given in the following paragraphs.

The local (Å-scale) variation of molecular mobility below T_{m2} drives the coexistence of two distinct molecular environments of the same G-C18:1-OH molecule. This occurs within a single-phase domain (as deduced by WAXS) of equivalent membrane rigidity (as derived from Laurdan probe in confocal microscopy). Although never reported before, the difference in the local mobility of the same amphiphile (here, G-C18:1-OH) could satisfy the theoretically-

559 required conditions, that induce local lipid segregation and formation of membrane inclusions
560 (Figure 8c). In case of their non-zero average orientation, the local membrane curvature
561 increases,[62] and nanotubes can spontaneously form (Figure 8b,c). More intriguing, this
562 mechanism occurs at least 10°C above T_{m1}, although it should not be favored above the T_m.[27]
563 From both experimental and theoretical backgrounds, the conditions of topologically-
564 connected vesicles-nanotubes systems are met only when either internal (two components), or
565 external, driving forces are applied.[19] In the present single-lipid system, of which the phase
566 behavior is summarized in Figure 8a, the most plausible driving force could be explained by
567 the NMR results collected on the dry sample. G-C18:1-OH concomitantly occupies two
568 molecular environments, characterized by: 1) two distinct conformations of the sugar
569 displaying equivalent mobility and 2) two conformations of the acyl chain unsaturation.
570

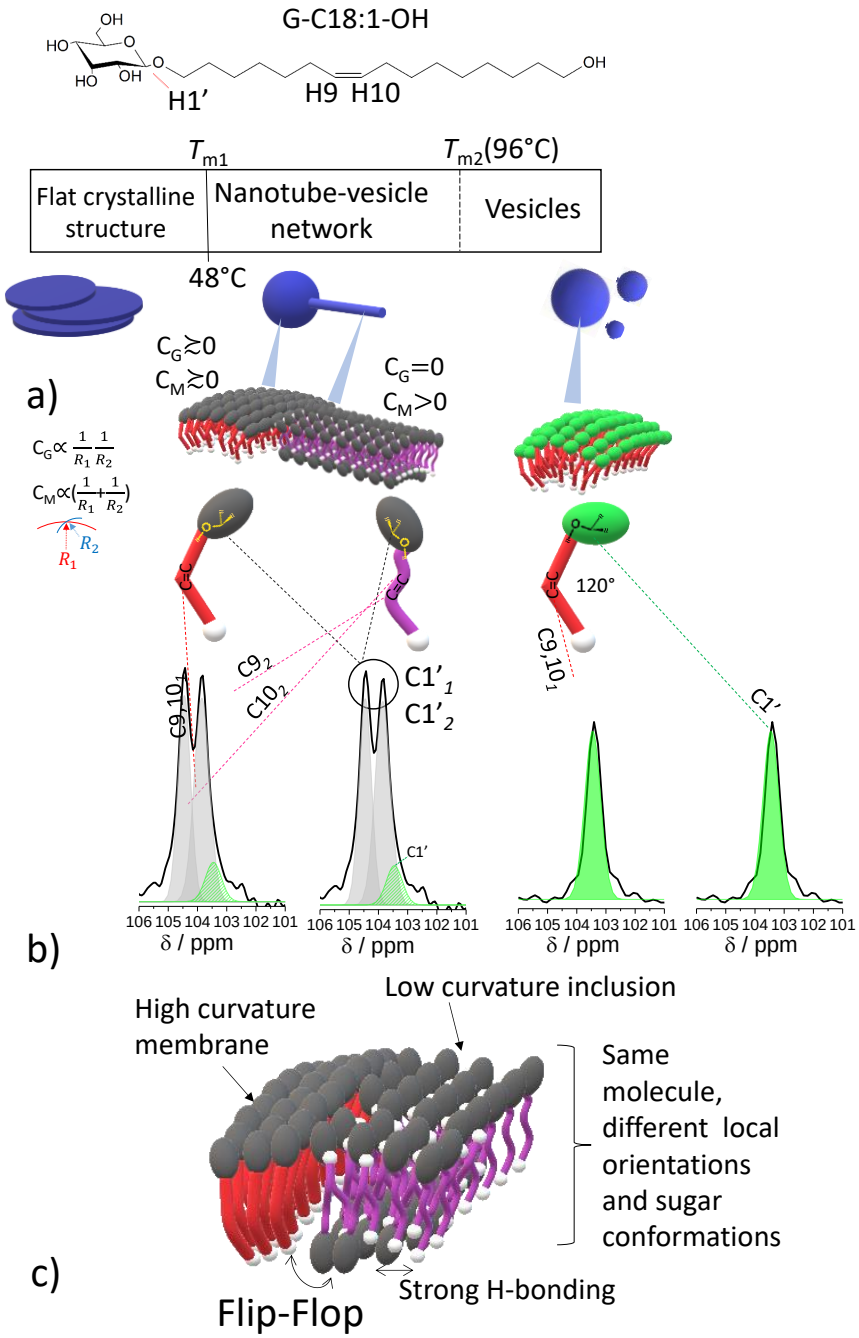

Figure 8 – a) Thermotropic phase behavior of G-C18:1-OH at 5 mg.mL^{-1}. Note that T_{m2} is observed on the dry powder, only. b) Possible relationship between the molecular environment, as derived from NMR, and membrane curvatures. All the molecular drawings refer to the same G-C18:1-OH molecule (bulky ellipsoid ≡ sugar headgroup), while each color corresponds to a given configuration. Grey of C1'$_1$ and C1'$_2$ indicates the uncertainty about the assignment of the specific NMR peak. The curvature, C, is defined as 1/R, R being the curvature radius. R_1, R_2: radius of curvature; C_G: Gauss curvature; C_M: Mean curvature. c) Free interpretation of the anisotropic, high-curvature ($C_M > 0$; $C_G = 0$), inclusions in the membrane (low C_M and C_G) continuum driven by inter-sugar H-bonding and reduced intramembrane diffusion for a G-C18:1-OH glucolipid.

Two related questions are unanswered at the moment. What actually drives nanotube formation and is the organization of G-C18:1-OH within the vesicles and tubes the same? Lipid nanotubes have been studied for at least three decades, over which broad experimental and theoretical insight has been generated. Despite this fact, the actual understanding is still matter of debate.[27] Micelle-to-nanotube and vesicle-to-nanotube phase transitions are generally reported for single amphiphiles below a given T_m and intermediate phase composed of twisted and flat fibers is concomitantly reported. Initially thought to be a chirality-driven phenomenon, recent studies propose a more general mechanism involving crystallization and symmetry breaking in the lipid packing driven by optimal packing.[27] If twisted ribbons were observed before for a number of microbial glycolipid bolaamphiphiles,[44] they are not found for G-C18:1-OH. This fact, as well as the large body of cryo-TEM images and the observation of nanotubes above T_{m1}, rather pledge in favour of a direct topological change from positive (vesicles) to zero (nanotubes) Gaussian curvatures. In this case, vesicle-to-nanotube transitions could be driven by external forces.[5,6,30,7,8,13–16,28,29]

Considering the absence of external forces in the present system, there are only two possibilities left, spontaneous budding of the membrane or nanotube pulling after inter-vesicle collisions due to Brownian motion. Both are possible, as inclusions composed of a different arrangement of the same molecule in the membrane continuum can theoretically explain spontaneous nanotube formation in an isotropic medium.[6,7,22,23,62,9–12,18–21] However, the second one is probably more likely to prevail, because it could explain the large number of nanotubes connecting two distant vesicles. Interestingly, similar events occur for any phospholipid-based vesicular solution, but nanotubes are extremely rare unless at least two lipids of different molecular structure are mixed together. The spectroscopic, ^{1}H and ^{13}C, and relaxation (^{1}H) ssNMR data, even if collected on a dry powder, demonstrate that the coexistence of two G-C18:1-OH configurations, involving both the sugar headgroup and fatty alcohol chain, are possible for this molecule. As a matter of fact, this is not so surprising, as more than one energy minima, each corresponding to a given conformation, are known for glucose, its non-reducing derivative, methylglucose, and carbohydrates in general.[78–80]

The presence of two configurations could explain the coexistence between two structures of different curvature, but the data presented so far do not explain the origin of these two configurations. In other words, what drives the change in the local structure of the sugar headgroup and fatty alcohol within the membrane?

The association of known self-assembled structures to spectroscopic ^{13}C ssNMR data is known for years, in particular for gluconamides, lipids having a linear sugar headgroup.[81–84] It

was found that *gauche* effects, in some cases up to the γ position, in the sugar chain induce upfield chemical shifts, while *anti* and *trans* conformations result in downfield shifts. Each structure (monolayer crystal, bilayer crystal or micellar fiber) was then characterized by a given organization of the gluconamide and a characteristic ^{13}C ssNMR fingerprint, which could be explained by *gauche*, *γ-gauche*, *anti* and *trans* conformations of the headgroup. Similar structural-spectroscopic correlations have been collected over the years for much simpler cyclic sugars,[85] whereas pyranoses can undergo important conformational changes (chair, half-chair, boat, skew), when the appropriate energy barriers are crossed.[78–80,86] A quantitative conformational study based on the ^{13}C chemical shift variations shown in Table 1 would be certainly helpful, but very delicate in the context of the present state of the art, because a rigorous approach requires at least one known crystal structure,[81,82] which is currently missing for this compound. A qualitative approach will then be adopted.

G-C18:1-OH is a bolaform amphiphile and flip-flop could be a possible mechanism involved in the nanotube stabilization, whereas head-tail interactions have long been considered as important in nanotube-forming bolaform amphiphiles.[60,63] From mere considerations based on T_2 (^1H) relaxation arguments, one could exclude head-tail configurations: if the R-C$\underline{H_2}$OH endgroup (H1) was involved in a direct interaction with the sugar group, its corresponding T_2 would probably be comparable to the sugar's one (OH and H1'), but this does not seem to be the case. However, this hypothesis would be based on the comparison of the relaxation from CH and CH_2 protons, additionally involved in different kind of motions. Besides, the relaxation of H1 is influenced by the strong overlap between H1 and H5'. For these reasons, relaxation arguments are not solid enough and will not be used.

We then address this question by exploring intermolecular interactions in a direct manner, using 2D ^1H-^1H homonuclear ssNMR correlation spectroscopy. At 90°C, in the fast-tumbling domain of molecular motion (narrow ^1H NM**R** peaks, Figure 6a) and corresponding to the vesicle-rich region, spin diffusion (NOESY) experiments are preferred over dipolar coupling based experiments, because such interaction is averaged out by molecular motion. However, when the molecular motion is more constrained, in the domain of nanotube stability at 70°C (broad ^1H spectra, Figure 6a), Double-Quantum Single-Quantum (DQ-SQ) correlation experiments are best suited to probe interaction between close molecular neighbors. These experiments are reported in Figure 9 and the related interpretation is only briefly reported below, while a more detailed discussion can be found on Page 12 in the Supporting Information.

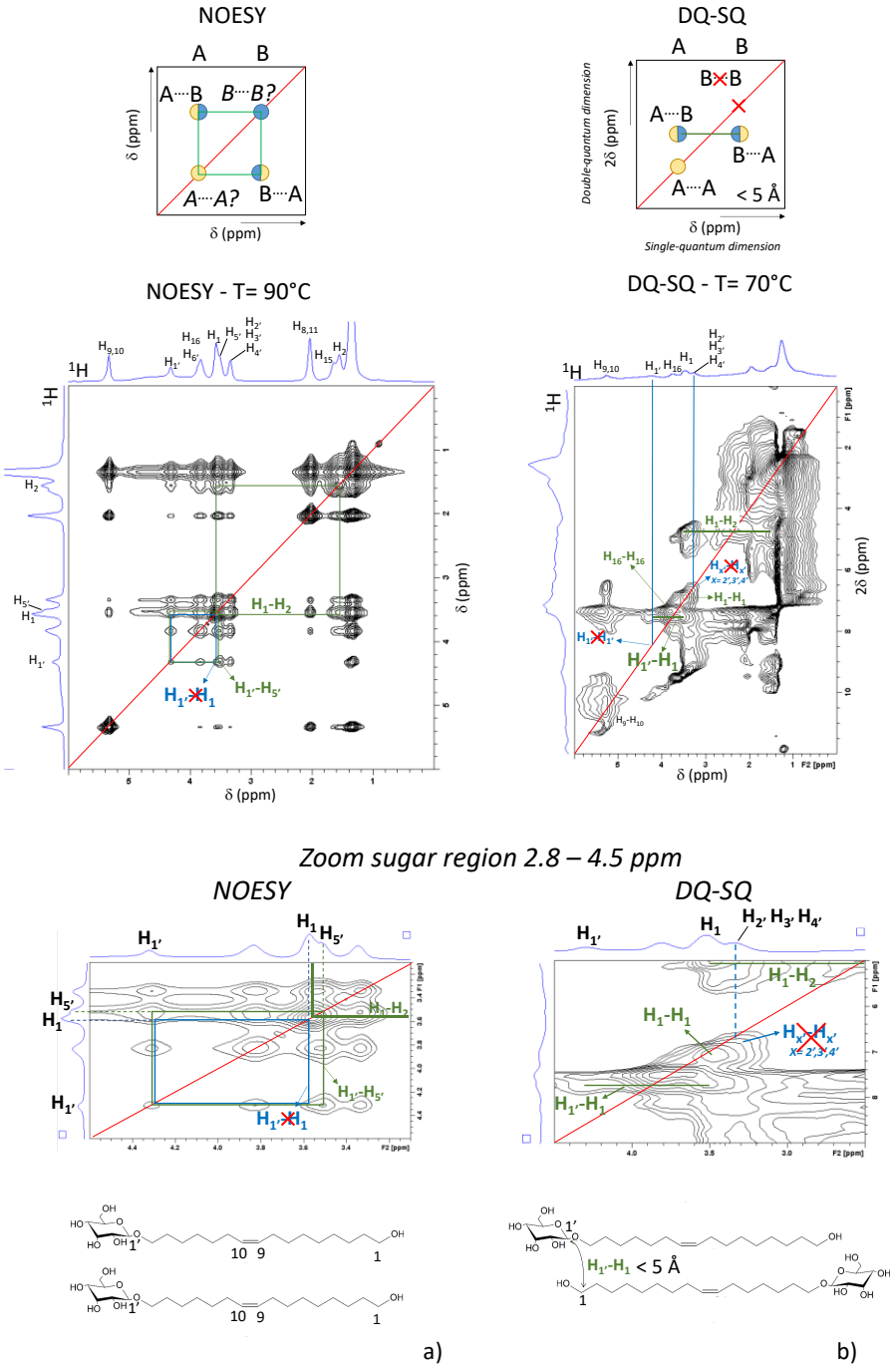

Figure 9 – a) 2D ^{1}H-^{1}H NOESY NMR experiment performed at MAS= 10 kHz (4 mm probe) on a Bruker 300 MHz Avance III HD spectrometer using 300 ms of mixing time. Sample temperature is regulated to 90°C, reached by cooling from 110°C. b) 2D ^{1}H-^{1}H DQ-SQ (BAck-to-BAck, BABA, pulse sequence used for the DQ excitation scheme) NMR experiment performed at MAS= 22 kHz (2.5 mm probe) on a Bruker 700 MHz Avance III spectrometer using a DQ excitation time equal to 2 rotor periods. Sample temperature is regulated to 70°C, reached by cooling from 110°C. The typical schemes illustrating how to interpret these 2D experiments are reported above each experimental map. Zooms of the sugar region and configurational interpretation are given below each 2D map. More information are given in the text below.

Head-tail or head-head configurations could be probed by the existence of H1'-H1 interactions, whereas H1 (δ_H= 3.56 ppm) is associated to the glucolipid tail and H1' (δ_H= 4.32 ppm) to the sugar headgroup. These atoms are more than 15 Å apart, and a direct interaction could not be observed in both NOESY and DQ-SQ experiments. NOESY experiments (Figure 9a) show that H1'-H1 correlations are not observed. Meanwhile, clear-cut, direct, H1'-H1 interactions are indeed observed are detected at T= 70°C (DQ cross-peaks related to H1'-H1 correlation in DQ-SQ experiment shown in Figure 9b). Interestingly, the absence of auto peaks at δ_H= 4.32 ppm and δ_H= 3.35 ppm in the SQ dimension excludes H1'-H1' and Hx'-Hx' (x= 2, 3, 4) interactions respectively, strengthening the idea that sugar headgroups from two nearest-neighbor G-C18:1-OH molecules are not adjacent in the nanotube-vesicle region.

Homonuclear 2D ssNMR supports the idea, according to which G-C18:1-OH can undergo molecular flip-flops and a head-tail arrangement in the dry product. Extrapolating these conclusions in the lower concentration range, lack of H1'-H1 proximity at T= 90°C suggests a head-head configuration in the vesicle-rich region and head-tail configuration within the nanotubes. It is however still unclear whether flip-flops are driven by spontaneous, temperature-induced, conformational changes in the glucolipid packing, stimulating inclusions within the membrane itself,[6,7,22,23,62,9–12,18–21] or by defects generated by inter-vesicle collisions. In fact, a combination of both is not unlikely. Nanotubes are not stable when temperature is 20 to 30 degrees above T_{m1}, indicating that inter-vesicle collisions alone cannot explain the unusual phenomenon. In an energy landscape approach,[87] the head-head configuration is certainly favored at high temperature, while both head-head and head-tail configurations could be favored in the mid-temperature region, corresponding to the range between T_{m1} and T_{m2} in the dry powder. Both statistical and defect-induced flip-flop events contribute to form high mean, zero Gaussian, curvature morphologies (nanotubes), for which the head-tail conformation, limiting the proximity between bulky sugar headgroups, is probably more adapted (Figure 8c). The flip-flop interpretation now reasonably explains the strong differences in the sugar and fatty alcohol conformations, deduced by the multiple NMR signals attributed to chemically-equivalent groups. The existence of various low-energy conformations, each having specific NMR signature, for sugars in solution[78–80,86] and solid-state[81–84] further supports our interpretation.

One last point should be clarified. Why, between T_{m1} and T_{m2}, are two molecular environments able to coexist, instead of a single one of average rigidity, as found in the case of "ripple" phases?[50–54] We believe that this question can be answered based on the NMR results: the relatively short T_2 values of the H1' and OH protons shows the constrained mobility of the

sugar headgroup, despite a certain flexibility of the chain (long T_2 component). This trend may suggest restrictions in translational mobility, probably due to the sugar-OH hydrogen bonding (Figure 8c), meaning that lipids are not able to diffuse within the membrane, thus keeping two different configurations stable.

Conclusions

Topologically-connected nanotube-vesicle lipidic systems are commonly observed for self-assembled membranes composed of at least two amphiphiles, and spontaneously driven by anisotropic inclusions and/or by external directional forces. This work shows that strong differences in membrane curvature can spontaneously occur in single-lipid systems without external anisotropic forces. Coexistence and interconnection between nanotubes and vesicles are evidenced via cryo-TEM and fluorescence confocal microscopy in a single-phase region at temperature above a transition temperature, T_{m1}= 48.3°C, determined by DSC on the hydrated sample, but below the second transition temperature, T_{m2} (95.7°C) determined by DSC on the dry powder. X-ray diffraction (WAXS) also shows the coexistence of two lattice periods, one attributed to an inter-membrane repeating distance and the other possibly related to the intra-nanotube glucolipid arrangement. Labelling the systems with Laurdan, a fluorophore of which the emission strongly varies with the local membrane rigidity, excludes the presence of rigid micro-separated phases (e.g., L_β).

^{1}H and ^{13}C ssNMR, despite the fact that it can only be performed on the dry powder, confirm the presence of one main fluid G-C18:1-OH environment above T_{m2}. Below T_{m2}, the splitting of some ^{13}C peaks and the coexistence of short and long ^{1}H relaxation components demonstrate that G-C18:1-OH can simultaneously pack into structurally and dynamically inequivalent environments. Combining advanced 2D ^{1}H-^{1}H correlation experiments based on spin diffusion or double-quanta excitation suggests that vesicles could contain a preferred head-head configuration of the bolaform lipid, while nanotubes a preferred head-tail assembly.

The presence of two environments composed of the same molecule characterized by different molecular configurations and rigidity fulfills the theoretical conditions necessary to spontaneously nucleate a membrane inclusion of non-zero average orientation, described as necessary to observe topologically-connected nanotube-vesicle structures in the absence of external forces. This hypothesis could also be enriched by the possibility of nanotubes to be pulled away between two vesicles after a collision event.

This work expands the actual theoretical and experimental framework on lipid networks stabilized by a different radius of curvature. It could also motivate the synthesis, or isolation,

of new lipids providing a higher level of 3D architectural control in soft networks, possibly in the range of room temperature.

Acknowledgements

Dr. Andrea Lassenberger and Dr. Sylvain Prévost at Institut Laue Langevin (ILL, Grenoble, France) are kindly acknowledged for their assistance on the SANS experiment. Confocal images were performed at the Institut de Biologie Paris Seine (IBPS) imaging facility. Jean-François Gilles (Imaging Core Facility, Institut de Biologie Paris Seine (IBPS), CNRS, Sorbonne Université, Paris, France) is kindly acknowledged for his assistance on the confocal microscopy imaging. Dr. Guillaume Laurent (LCMCP, Sorbonne Université, Paris, France) is kindly acknowledged for helpful discussions. The French region Ile-de-France SESAME program is acknowledged for financial support (700 MHz NMR spectrometer). Dr. Olivier Diat (ICSM, Marcoule, France), Prof. Aleš Iglič and Prof. Veronika Kralj-Iglič (University of Ljubljana, Slovenia) are kindly acknowledged for helpful discussions.

Financial support

WAXS experiments have been supported by Soleil Light Source, Saint Aubin, France, proposal N° 20201747. SANS experiments have been supported by ILL, proposal N°9-13-778.

References

1 D. Kabaso, N. Bobrovska, W. Góźdź, E. Gongadze, V. Kralj-Iglič, R. Zorec and A. Iglič, *Bioelectrochemistry*, 2012, **87**, 204–210.

2 C. R. Safinya, U. Raviv, D. J. Needleman, A. Zidovska, M. C. Choi, M. A. Ojeda-Lopez, K. K. Ewert, Y. Li, H. P. Miller, J. Quispe, B. Carragher, C. S. Potter, M. W. Kim, S. C. Feinstein and L. Wilson, *Adv. Mater.*, 2011, **23**, 2260–2270.

3 P. Veranič, M. Lokar, G. J. Schütz, J. Weghuber, S. Wieser, H. Hägerstrand, V. Kralj-Iglič and A. Iglič, *Biophys. J.*, 2008, **95**, 4416–4425.

4 A. Rustom, R. Saffrich, I. Markovic, P. Walther and H.-H. Gerdes, *Science (80-.).*, 2004, **303**, 1007–1010.

5 M. I. Angelova, S. Soléau, P. Méléard, F. Faucon and P. Bothorel, *Prog. Colloid Polym. Sci.*, 1992, **89**, 127–131.

6 L. Mathivet, S. Cribier and P. F. Devaux, *Biophys. J.*, 1996, **70**, 1112–1121.

7 V. Kralj-Iglič, G. Gomišček, J. Majhenc, V. Arrigler and S. Svetina, *Colloids Surfaces A Physicochem. Eng. Asp.*, 2001, **181**, 315–318.

8 V. Kralj-Iglič, A. Iglič, G. Gomišček, F. Sevšek, V. Arrigler and H. Hägerstrand, *J. Phys. A. Math. Gen.*, 2002, **35**, 1533–1549.

9 M. Drab, D. Stopar, V. Kralj-Iglič and A. Iglič, *Cells*, 2019, **8**, 626.

10 A. Zidovska, K. K. Ewert, J. Quispe, B. Carragher, C. S. Potter and C. R. Safinya, *Langmuir*, 2009, **25**, 2979–2985.

11 A. Zidovska, K. K. Ewert, J. Quispe, B. Carragher, C. S. Potter and C. R. Safinya, *Soft Matter*, 2011, **7**, 8363–8369.

12 A. Zidovska, K. K. Ewert, J. Quispe, B. Carragher, C. S. Potter and C. R. Safinya, *Biochim. Biophys. Acta - Biomembr.*, 2009, **1788**, 1869–1876.

13 M. Karlsson, K. Sott, M. Davidson, A. S. Cans, P. Linderholm, D. Chiu and O. Orwar, *Proc. Natl. Acad. Sci. U. S. A.*, 2002, **99**, 11573–11578.

14 A. Karlsson, R. Karlsson, M. Karlsson, A.-S. Cans, A. Stromberg, F. Ryttsen and O. Orwar, *Nature*, 2001, **409**, 150–152.

15 M. Karlsson, K. Sott, A. S. Cans, A. Karlsson, R. Karlsson and O. Orwar, *Langmuir*, 2001, **17**, 6754–6758.

16 E. Evans, H. Bowman, A. Leung, D. Needham and D. Tirrell, *Science (80-.).*, 1996, **273**, 933–935.

17 U. Seifert, *Configurations of fluid membranes and vesicles*, 1997, vol. 46.

18 J. Käs and E. Sackmann, *Biophys. J.*, 1991, **60**, 825–844.

19 N. Bobrovska, W. Góźdź, V. Kralj-Iglič and A. Iglič, *PLoS One*, 2013, **8**, e73941.

20 A. Iglič, B. Babnik, K. Bohinc, M. Fošnarič, H. Hägerstrand and V. Kralj-Iglič, *J. Biomech.*, 2007, **40**, 579–585.

21 K. Bohinc, T. Slivnik, A. Iglič, M. Brumen and V. Kralj-Iglič, *J. Phys. Chem. C*, 2007, **111**, 9709–9718.

22 A. Iglič, H. Hägerstrand, P. Veranič, A. Plemenitaš and V. Kralj-Iglič, *J. Theor. Biol.*, 2006, **240**, 368–373.

23 V. Kralj-Iglič and P. Veranič, *Adv. Planar Lipid Bilayers Liposomes*, 2006, **5**, 129–149.

24 A. Iglic and V. Kralj-Iglic, *Adv. Planar Lipid Bilayers Liposomes*, 2006, **4**, 253–279.

25 S. Penič, L. Mesarec, M. Fošnarič, L. Mrówczyńska, H. Hägerstrand, V. Kralj-Iglič and A. Iglič, *Front. Phys.*, 2020, **8**, 342.

26 P. Yager and P. E. Schoen, *Mol. Cryst. Liq. Cryst.*, 1984, **106**, 371–381.

27 T. G. Barclay, K. Constantopoulos and J. Matisons, *Chem. Rev.*, 2014, **114**, 10217–10291.

28 B. Božič, G. Gomišček, V. Kralj-Iglič, S. Svetina and B. Žekš, *Eur. Biophys. J.*, 2002, **31**, 487–496.
29 A. Iglič, H. Hägerstrand, M. Bobrowska-Hägerstrand, V. Arrigler and V. Kralj-Iglič, *Phys. Lett. A*, 2003, **310**, 493–497.
30 R. Bar-Ziv and E. Moses, *Phys. Rev. Lett.*, 1994, **73**, 1392–1395.
31 S. Chiruvolu, H. E. Warriner, E. Naranjo, S. H. Idziak, J. O. Rädler, R. J. Plano, J. A. Zasadzinski and C. R. Safinya, *Science (80-.).*, 1994, **266**, 1222–1225.
32 V. Kralj-Iglič, A. Iglič, H. Hägerstrand and P. Peterlin, *Phys. Rev. E*, 2000, **61**, 4230–4234.
33 L. Mesarec, M. Drab, S. Penič, V. Kralj-Iglič and A. Iglič, *Int. J. Mol. Sci.*, 2021, **22**, 2348.
34 L. Van Renterghem, S. L. K. W. Roelants, N. Baccile, K. Uyttersprot, M. C. Taelman, B. Everaert, S. Mincke, S. Ledegen, S. Debrouwer, K. Scholtens, C. V. Stevens, W. Soetaert, L. Van Renterghem, S. L. K. W. Roelants, N. Baccile, K. Uytersprot, M. C. Taelman, B. Everaert, S. Mincke, S. Ledegen, S. Debrouwer, K. Scholtens, C. V. Stevens and W. Soetaert, *Biotechnol. Bioeng.*, 2018, **115**, 1195–1206.
35 J. Clark and F. Deswarte, *Introduction to Chemicals from Biomass: Second Edition*, John Wiley & Sons, 2015.
36 K. V. Sajna, R. Höfer, R. K. Sukumaran, L. D. Gottumukkala and A. Pandey, in *Industrial Biorefineries and White Biotechnology*, eds. A. Pandey, R. Höfer, M. Taherzadeh, K. M. Nampoothiri and C. Larroche, Amsterdam, Oxford, Waltham, Elsevier., 2015, pp. 499–521.
37 R. Marchant and I. M. Banat, *Trends Biotechnol.*, 2012, **30**, 558–565.
38 K. Hill and C. LeHen-Ferrenbach, in *Sugar-Based Surfactants: Fundamentals and Applications*, ed. C. C. Ruiz, Boca Raton, CRC Press., 2009, pp. 1–20.
39 L. Rodrigues, I. M. Banat, J. Teixeira and R. Oliveira, *J. Antimicrob. Chemother.*, 2006, **57**, 609–618.
40 J. D. Desai and I. M. Banat, *Microbiol. Mol. Biol. Rev.*, 1997, **61**, 47–64.
41 S. L. K. W. Roelants, K. Ciesielska, S. L. De Maeseneire, H. Moens, B. Everaert, S. Verweire, Q. Denon, B. Vanlerberghe, I. N. A. Van Bogaert, P. Van der Meeren, B. Devreese and W. Soetaert, *Biotechnol. Bioeng.*, 2016, **113**, 550–559.
42 N. Baccile, M. Selmane, P. Le Griel, S. Prévost, J. Perez, C. V. Stevens, E. Delbeke, S. Zibek, M. Guenther, W. Soetaert, I. N. A. Van Bogaert and S. Roelants, *Langmuir*, 2016, **32**, 6343–6359.

827 43 N. Baccile, A.-S. Cuvier, S. Prévost, C. V Stevens, E. Delbeke, J. Berton, W. Soetaert,
828 I. N. A. Van Bogaert and S. Roelants, *Langmuir*, 2016, **32**, 10881–10894.
829 44 N. Baccile, C. Seyrig, A. Poirier, S. A. Castro, S. L. K. W. Roelants and S. Abel, *Green*
830 *Chem.*, 2021, **23**, 3842–3944.
831 45 A. Salis, L. Cappai, C. Carucci, D. F. Parsons and M. Monduzzi, *J. Phys. Chem. Lett.*,
832 2020, **11**, 6805–6811.
833 46 J. Schindelin, I. Arganda-Carreras, E. Frise, V. Kaynig, M. Longair, T. Pietzsch, S.
834 Preibisch, C. Rueden, S. Saalfeld, B. Schmid, J.-Y. Tinevez, D. J. White, V.
835 Hartenstein, K. Eliceiri, P. Tomancak and A. Cardona, *Nat. Methods*, 2012, **9**, 676–
836 682.
837 47 T. Parasassi and E. Gratton, *J. Fluoresc.*, 1995, **5**, 59–69.
838 48 M. M. Dodes Traian, F. L. González Flecha and V. Levi, *J. Lipid Res.*, 2012, **53**, 609–
839 616.
840 49 D. M. Owen, C. Rentero, A. Magenau, A. Abu-Siniyeh and K. Gaus, *Nat. Protoc.*,
841 2012, **7**, 24–35.
842 50 W. Stillwell, in *An Introduction to Biological Membranes*, Academic Press, 2016, pp.
843 135–180.
844 51 W. Stillwell, in *An Introduction to Biological Membranes*, Academic Press, 2016, pp.
845 181–220.
846 52 B. Tenchov, *Chem. Phys. Lipids*, 1991, **57**, 165–177.
847 53 R. Koynova and M. Caffrey, *Biochim. Biophys. Acta*, 1998, **1376**, 91–145.
848 54 F. Schmid, S. Dolezel, O. Lenz and S. Meinhardt, *J. Phys. Conf. Ser.*, 2014, **487**,
849 012004.
850 55 S. Meinhardt, R. L. C. Vink and F. Schmid, *Proc. Natl. Acad. Sci. U. S. A.*, 2013, **110**,
851 4476–4481.
852 56 O. Glatter and O. Kratky, *Small Angle X-ray Scattering*, Academic Press, London,
853 1982.
854 57 B. A. Cunningham, A. D. Brown, D. H. Wolfe, W. P. Williams and A. Brain, *Phys.*
855 *Rev. E*, 1998, **58**, 3662–3672.
856 58 M. Nadler, A. Steiner, T. Dvir, O. Szekely, P. Szekely, A. Ginsburg, R. Asor, R. Resh,
857 C. Tamburu, M. Peres and U. Raviv, *Soft Matter*, 2011, **7**, 1512–1523.
858 59 C. Tanford, *The hydrophobic effect: Formation of micelles and biological membranes*,
859 John Wiley & Sons Inc, New York, 1973.
860 60 M. Masuda and T. Shimizu, *Langmuir*, 2004, **20**, 5969–5977.

61 A. Zidovska, K. K. Ewert, J. Quispe, B. Carragher, C. S. Potter and C. R. Safinya, *Block Liposomes. Vesicles of Charged Lipids with Distinctly Shaped Nanoscale Sphere-, Pear-, Tube-, or Rod-Segments*, Elsevier Inc., 1st edn., 2009, vol. 465.
62 A. Iglič, V. Kralj-Iglič, B. Božič, M. Bobrowska-Hägerstrand, B. Isomaa and H. Hägerstrand, *Bioelectrochemistry*, 2000, **52**, 203–211.
63 T. Shimizu, M. Masuda and H. Minamikawa, *Chem. Rev.*, 2005, **105**, 1401–1444.
64 J. V. Selinger and J. M. Schnur, *Phys. Rev. Lett.*, 1993, **71**, 4091–4094.
65 J. M. Schnur, *Science (80-.).*, 1993, **262**, 1669–1676.
66 B. Tenchov, R. Koynova and G. Rapp, *Biophys. J.*, 2001, **80**, 1873–1890.
67 R. Koynova and B. Tenchov, *Ser. Biomech.*, 2017, **31**, 3–19.
68 S. J. Angyal and R. Le Fur, *Carbohydr. Res.*, 1984, **126**, 15–26.
69 J. K. Whitesell and M. A. Minton, *J. Am. Chem. Soc.*, 1987, **109**, 225–228.
70 T. Takayama, S. Ando and I. Ando, *J. Mol. Struct.*, 1990, **220**, 245–250.
71 K. Gawrisch, N. V. Eldho and I. V. Polozov, *Chem. Phys. Lipids*, 2002, **116**, 135–151.
72 F. Tielens, C. Gervais, J. F. Lambert, F. Mauri and D. Costa, *Chem. Mater.*, 2008, **20**, 3336–3344.
73 G. A. Jeffrey and Y. Yeon, *Acta Crystallogr. Sect. B*, 1986, **42**, 410–413.
74 B. Berglund and R. W. Vaughan, *J. Chem. Phys.*, 1980, **73**, 2037–2043.
75 C. Gervais, C. Coelho, T. Azaïs, J. Maquet, G. Laurent, F. Pourpoint, C. Bonhomme, P. Florian, B. Alonso, G. Guerrero, P. H. Mutin and F. Mauri, *J. Magn. Reson.*, 2007, **187**, 131–140.
76 C. Akita, T. Kawaguchi, F. Kaneko, H. Yamamoto and M. Suzuki, *J. Phys. Chem. B*, 2004, **108**, 4862–4868.
77 R. N. Purusottam, L. Sénicourt, J. J. Lacapère and P. Tekely, *Biochim. Biophys. Acta - Biomembr.*, 2015, **1848**, 3134–3139.
78 X. Biarnés, A. Ardèvol, A. Planas, C. Rovira, A. Laio and M. Parrinello, *J. Am. Chem. Soc.*, 2007, **129**, 10686–10693.
79 L. M. J. Kroon-Batenburg and J. Kroon, *Biopolymers*, 1990, **29**, 1243–1248.
80 K. N. Kirschner and R. J. Woods, *Proc. Natl. Acad. Sci. U. S. A.*, 2001, **98**, 10541–10545.
81 S. Svenson, B. Kirste and J. H. Fuhrhop, *J. Am. Chem. Soc.*, 1994, **116**, 11969–11975.
82 I. Sack, S. Macholl, J. H. Fuhrhop and G. Buntkowsky, *Phys. Chem. Chem. Phys.*, 2000, **2**, 1781–1788.
83 S. Svenson, J. Koening and J. H. Fuhrhop, *J. Phys. Chem.*, 1994, **98**, 1022–1028.

84 S. Svenson, A. Schaefer and J. H. Fuhrhop, *J. Chem. Soc. Perkin Trans. 2*, 1994, **2**, 1023–1028.
85 K. Bock and C. Pedersen, *Adv. Carbohydr. Chem. Biochem.*, 1983, **41**, 27–66.
86 T. B. Grindley, *Structure and Conformation of Carbohydrates*, Springer, Berlin Heidelberg, 2008.
87 F. Tantakitti, J. Boekhoven, X. Wang, R. V. Kazantsev, T. Yu, J. Li, E. Zhuang, R. Zandi, J. H. Ortony, C. J. Newcomb, L. C. Palmer, G. S. Shekhawat, M. O. De La Cruz, G. C. Schatz and S. I. Stupp, *Nat. Mater.*, 2016, **15**, 469–476.

Supporting Information

Topological connection between vesicles and nanotubes in single-component lipid membranes driven by head-tail interactions

Niki Baccile,[a,*] Cédric Lorthioir,[a] Abdoul Aziz Ba,[a] Patrick Le Griel,[a] Cristina Coelho,[b] Javier Perez,[c] Wim Soetaert,[d] Sophie L. K. W. Roelants[d]

[a] Sorbonne Université, Centre National de la Recherche Scientifique, Laboratoire de Chimie de la Matière Condensée de Paris, LCMCP, F-75005 Paris, France

[b] Institut des Matériaux de Paris Centre, Sorbonne Université, Paris, France

[c] Synchrotron Soleil, L'Orme des Merisiers, Saint-Aubin, BP48, 91192 Gif-sur-Yvette Cedex, France

[d] InBio, Department of Biotechnology, Ghent University, Ghent, Belgium

*** Corresponding author:**

Dr. Niki Baccile

E-mail address: niki.baccile@sorbonne-universite.fr

Phone: +33 1 44 27 56 77

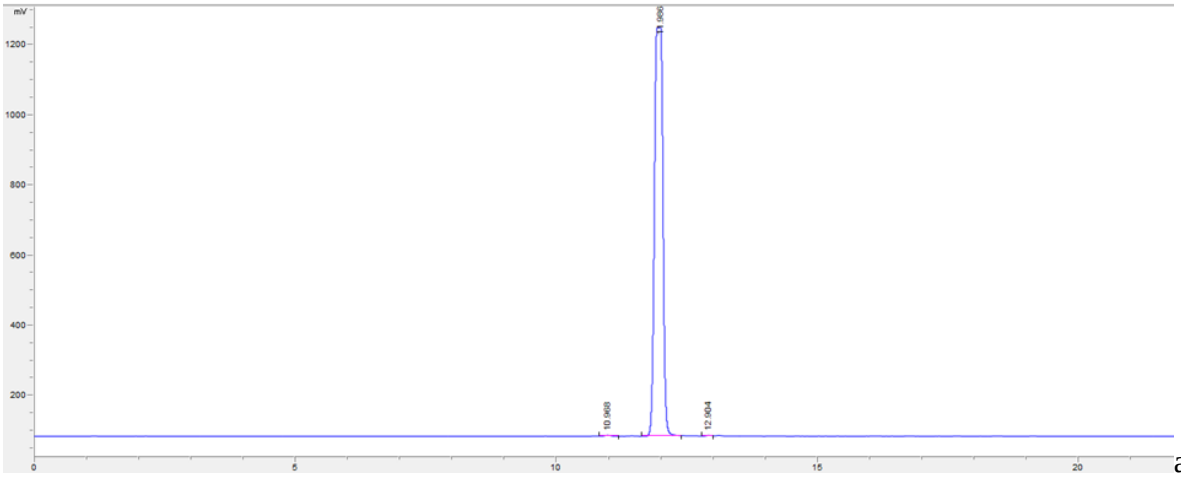

a)

Parameter		Method
Dry Matter (DM %)	99.6	Infrared balance 105°C
Glucose (%)	0.12	HPLC-Metacarb
Glycerol (%)	n.d.*	HPLC-Metacarb
Free Fatty Acid content (%)	<0.01	Internal method BBEPP: GC with FID Detector
Oil (%)	<0.01	Internal method BBEPP: GC with FID Detector
Moulds (CFU/g)	<10	3M-Nordval n°16 B
Yeasts (CFU/g)	<10	3M-Nordval n°16 B
Anaerobic count (CFU/g)	<10	SP-VG M005 B
Protein (%)	t.b.d.*	BCA protein assay

Figure S 1 - a) HPLC-ELSD chromatogram and composition table.

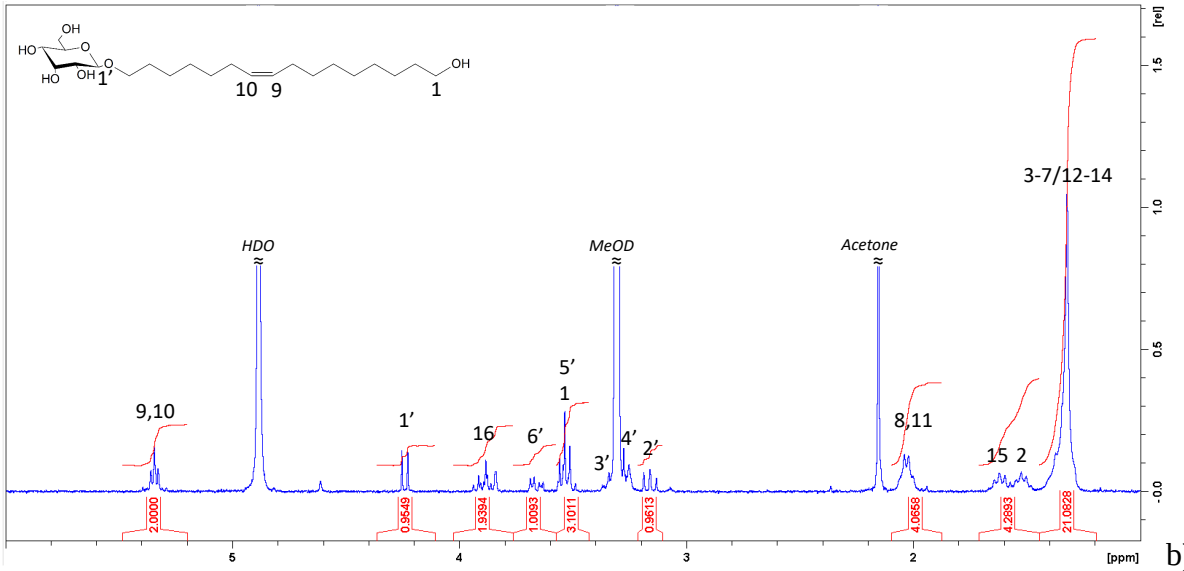

934 b)

935

Group	N°	δ / ppm
CH_2	1	3.54
CH_2	2	1.53
CH_2	3-7/12-14	1.32
CH_2	8,11	2.03
CH	9,10	5.34
CH_2	15	1.62
CH_2	16	3.88
CH	1'	4.24
CH	2'	3.16
CH	3'	3.34
CH	4'	3.29
CH	5'	3.54
CH_2	6'	3.66

936 **Figure S 1 (next) – b) ^{1}H NMR spectrum (MeOD-d4) recorded on the purified G-C18:1-OH compounds**
937 **and related assignment**

938

939

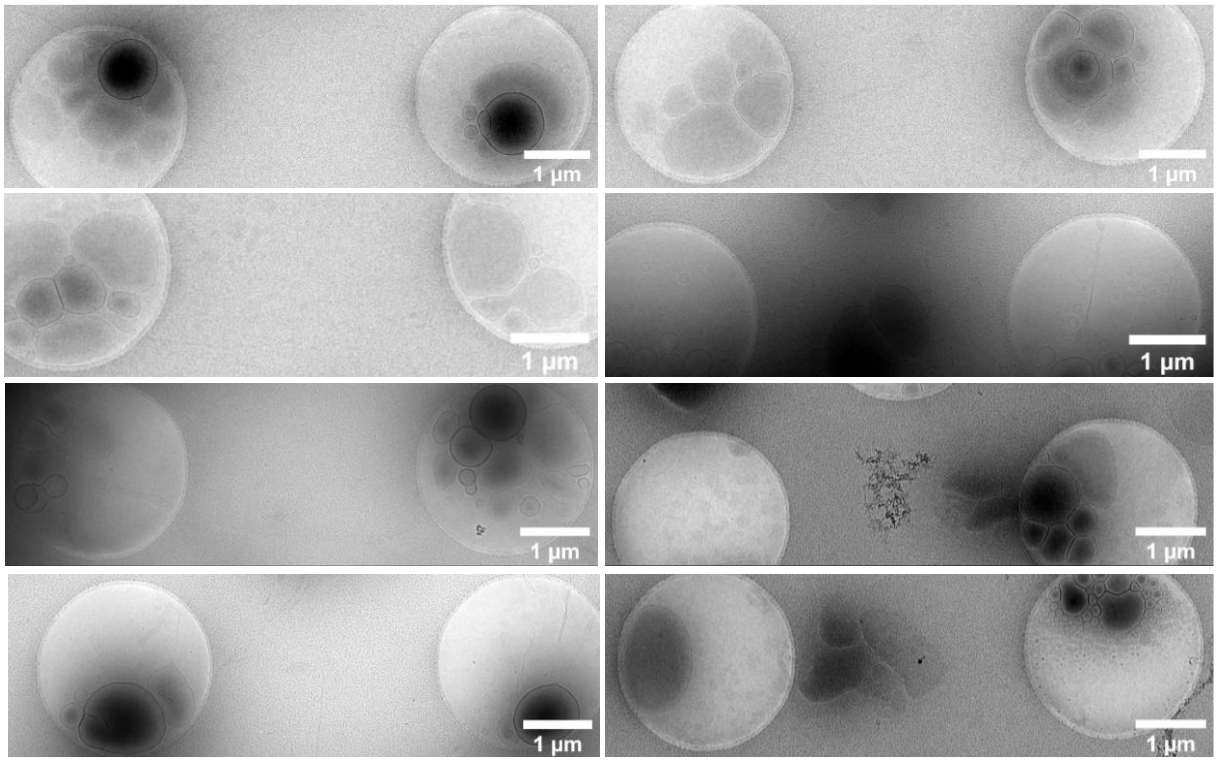

940

941 **Figure S 2 – Cryo-TEM images recorded for a 5 mg/mL G-C18:1-OH aqueous solution heat at *T**= 130°C.**

942

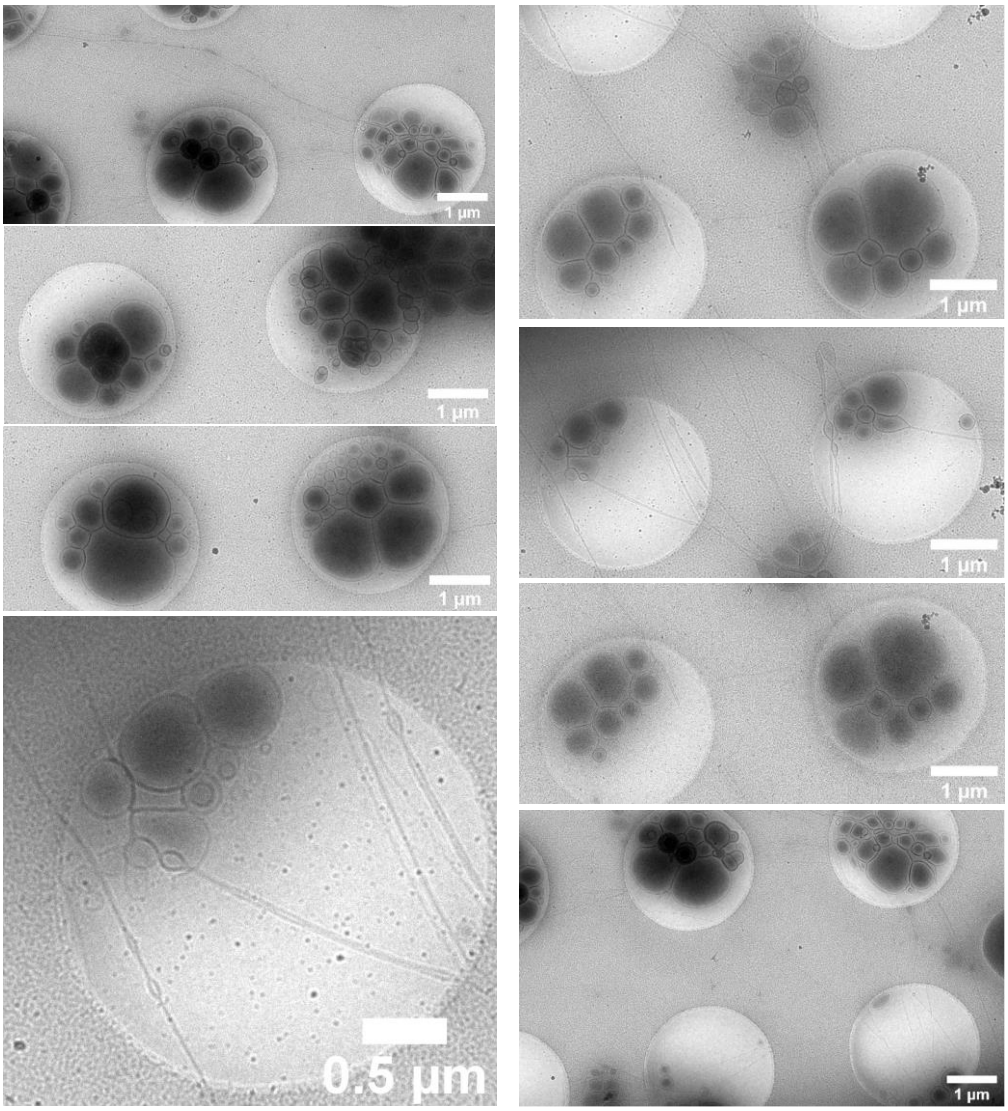

943

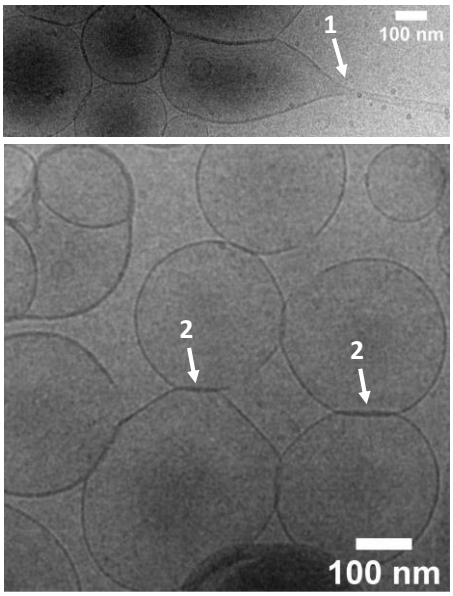

944 **Figure S 3 - Cryo-TEM images recorded for a 5 mg/mL G-C18:1-OH aqueous solution heat at *T**= 90°C.**

945

946
947
948
949
950
951

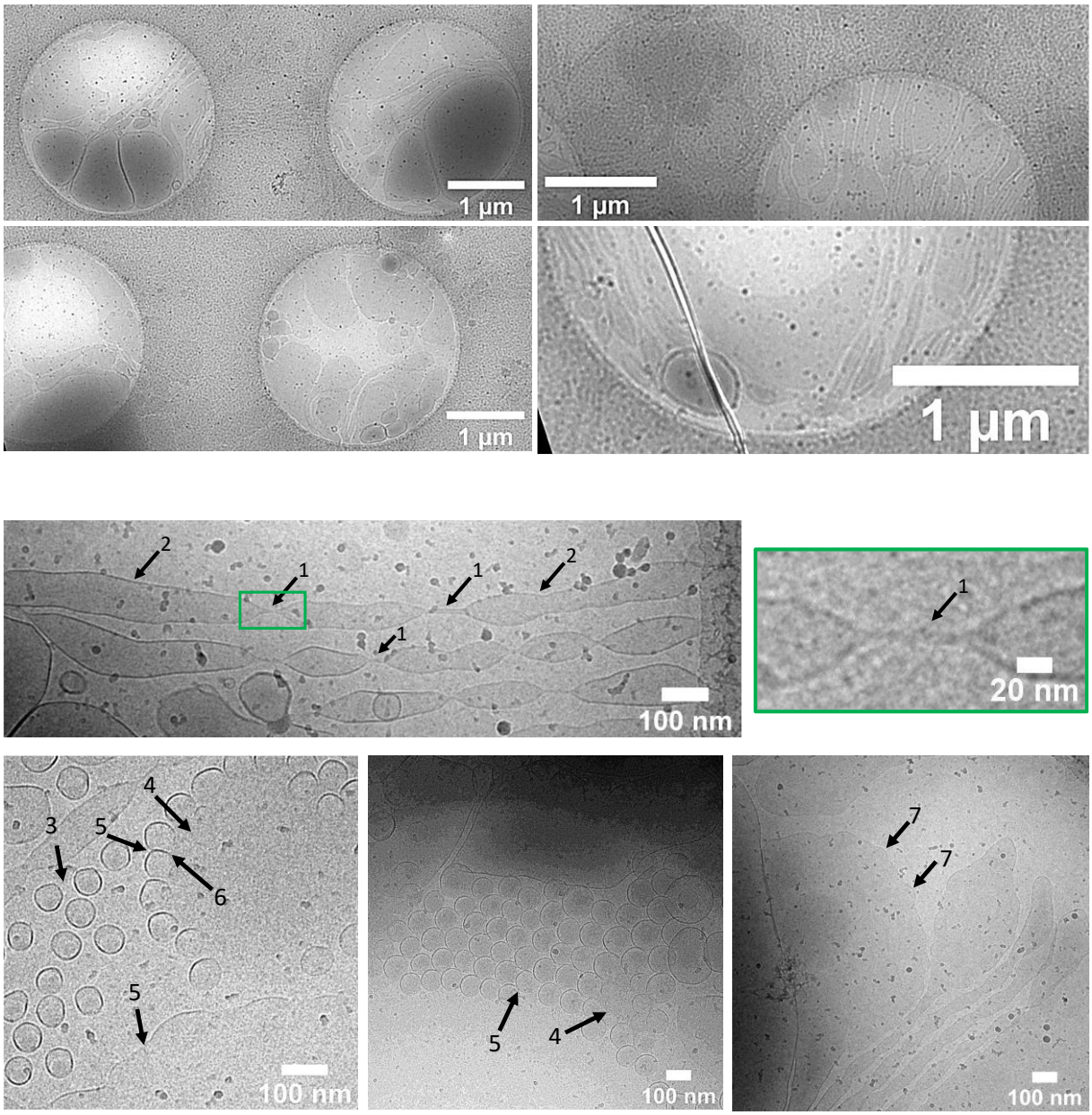

Figure S 4 – Cryo-TEM images recorded for a 5 mg/mL G-C18:1-OH aqueous solution heat at *T= 70°C.**

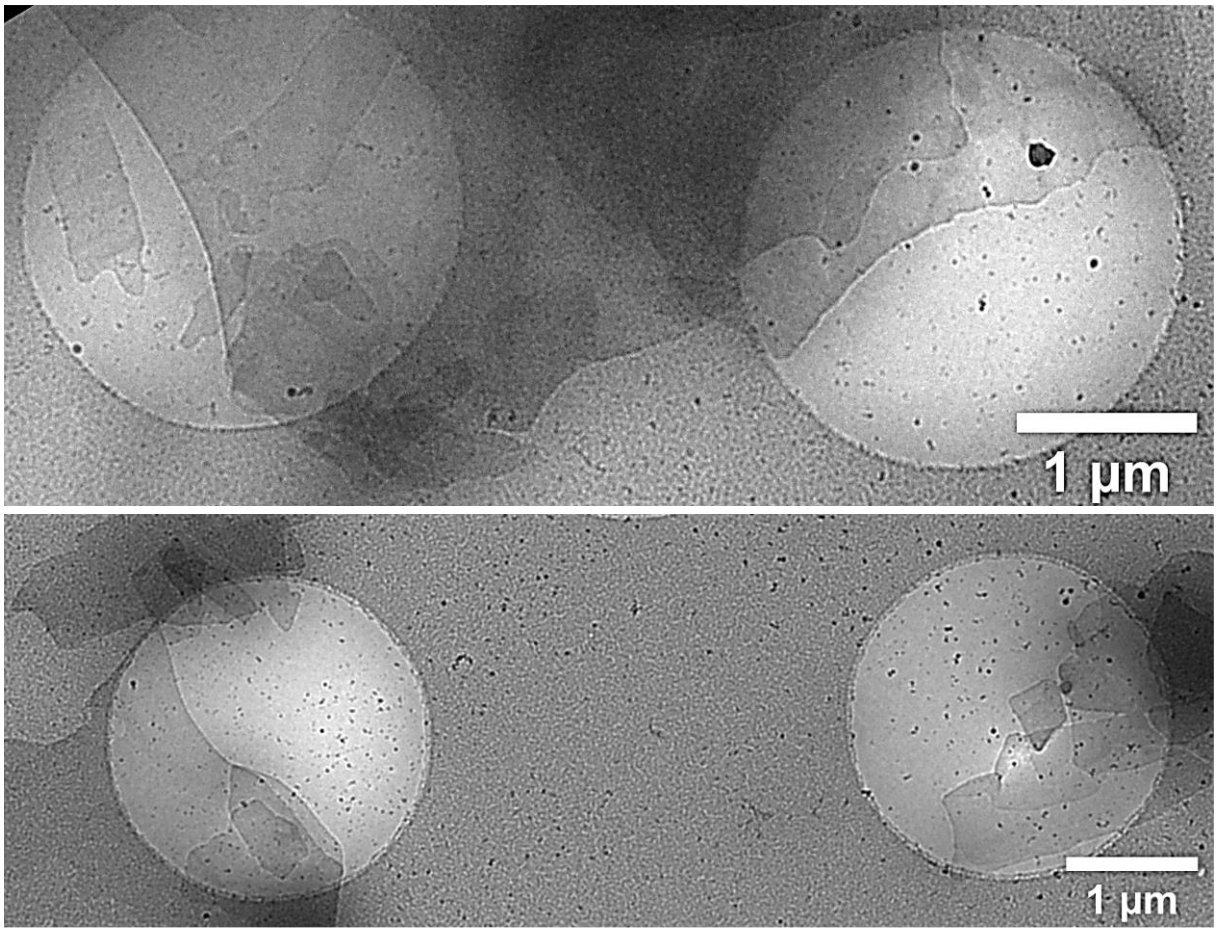

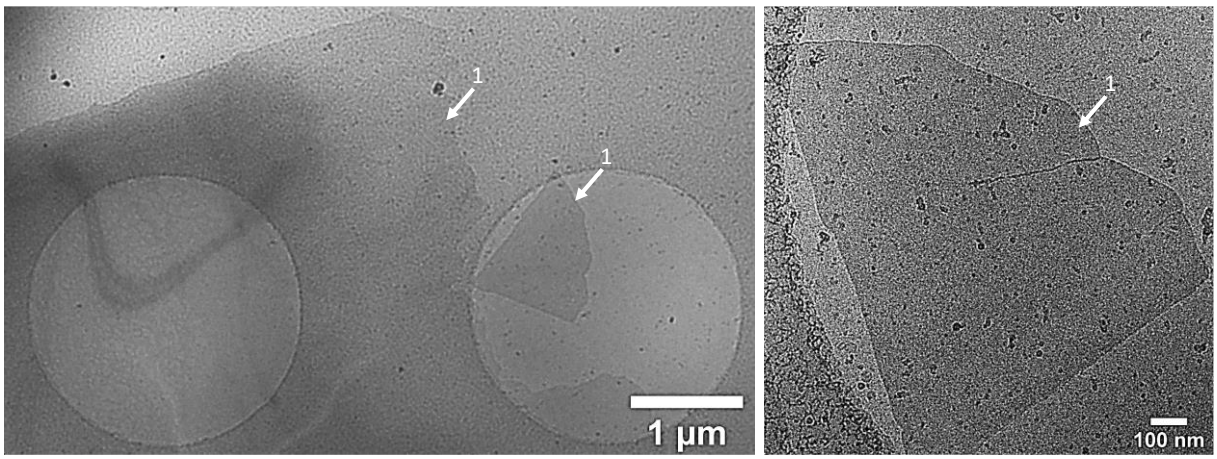

Figure S 5 – Cryo-TEM images recorded for a 5 mg/mL G-C18:1-OH aqueous solution heat at *T= 25°C.**

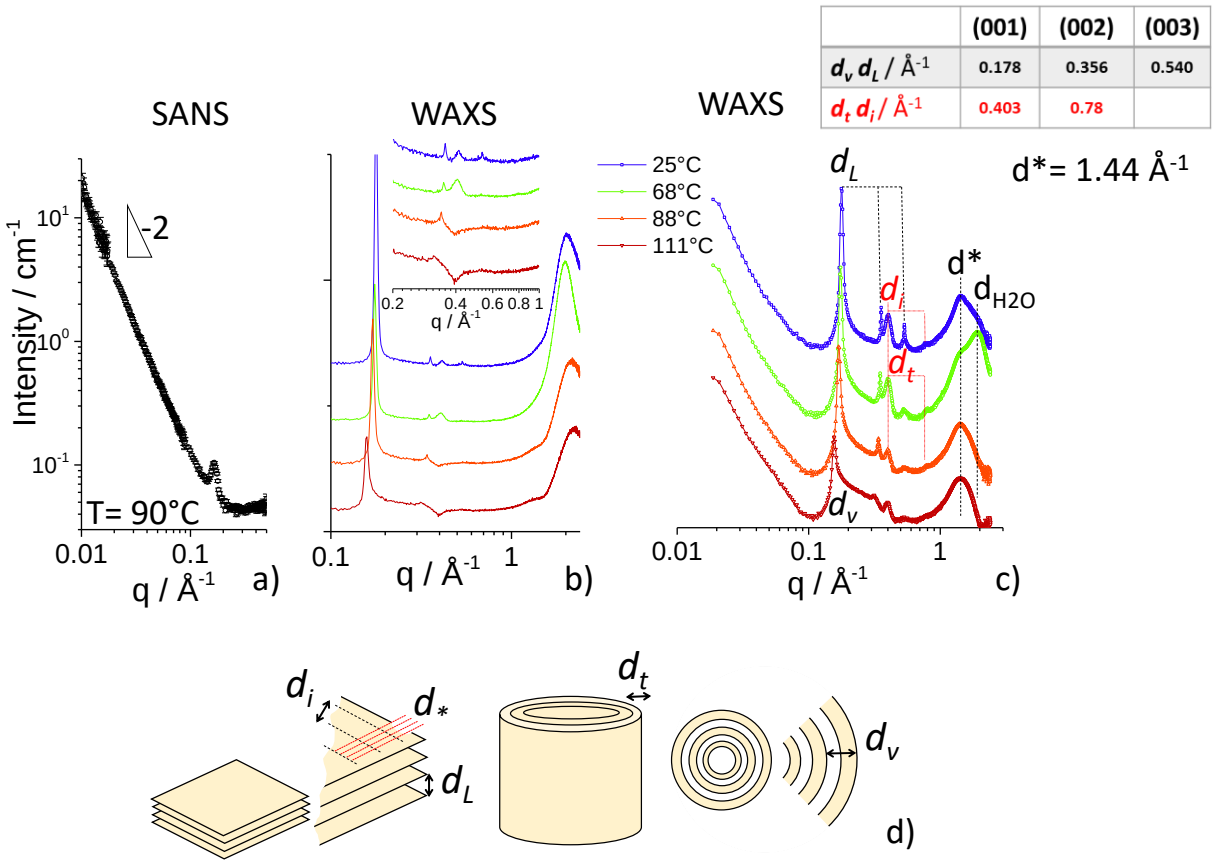

	(001)	(002)	(003)
d_v d_L / Å^{-1}	0.178	0.356	0.540
d_t d_i / Å^{-1}	0.403	0.78	

Figure S 6 – a) SANS experiment recorded at 90°C for a 5 mg/mL G-C18:1-OH aqueous solution. b-c) WAXS experiments recorded on aqueous solutions of G-C18:1-OH at b) 5 mg/mL and c) 25 mg/mL. d) Structural interpretation of the repeating distances pointed out in c).

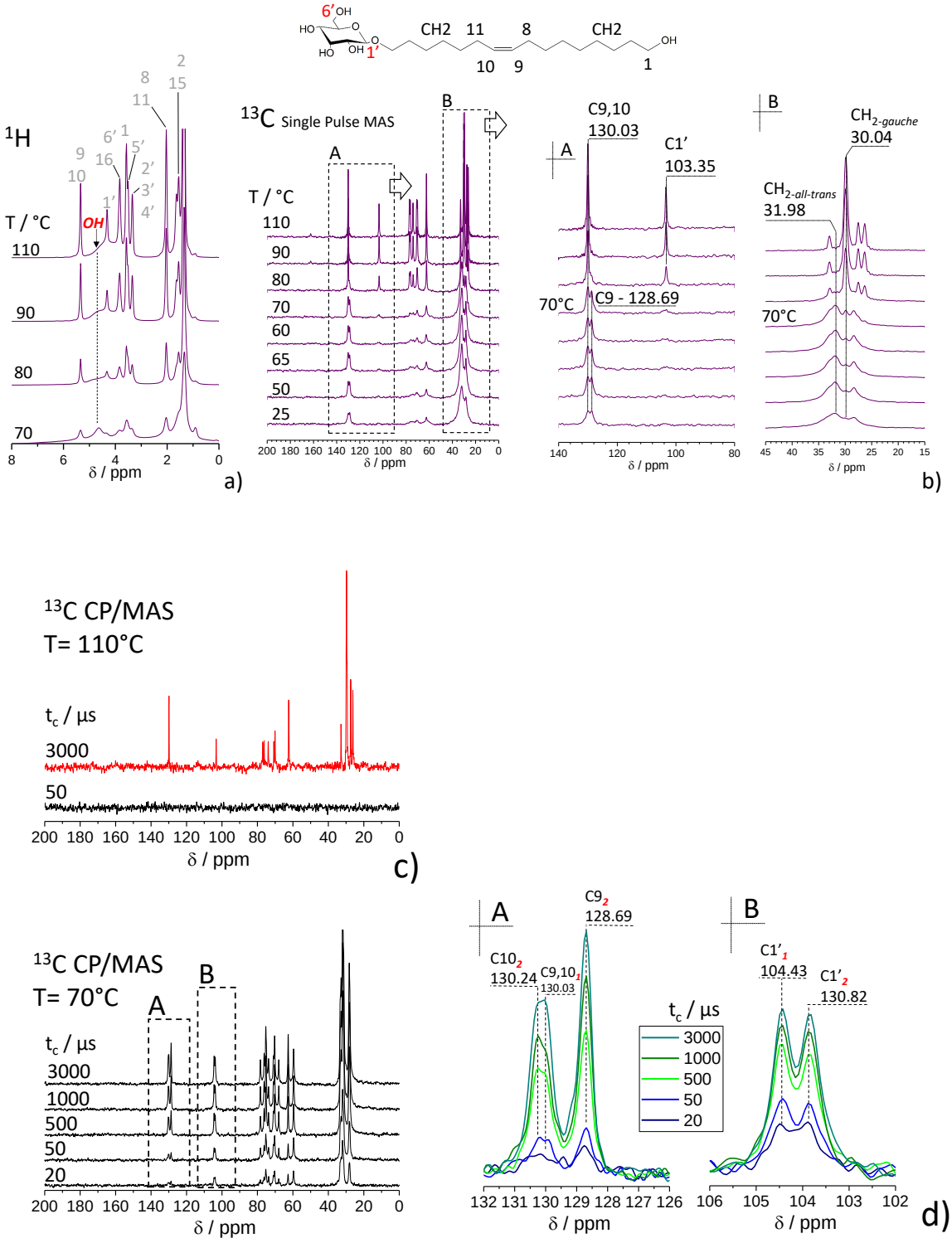

Figure S 7 – ssNMR MAS (10 kHz) experiments recorded on a G-C18:1-OH dry powder. a) ^{1}H spectra recorded from 110°C to 70°C. b) ^{13}C single pulse (SP) spectra recorded with high power ^{1}H decoupling from 110°C to 70°C. c) ^{13}C cross polarization (CP) spectra recorded at 110°C and contact time, t_c, of 50 µs and 3000 µs. d) ^{13}C CP spectra recorded at 70°C and for 20 < t_c / µs < 3000

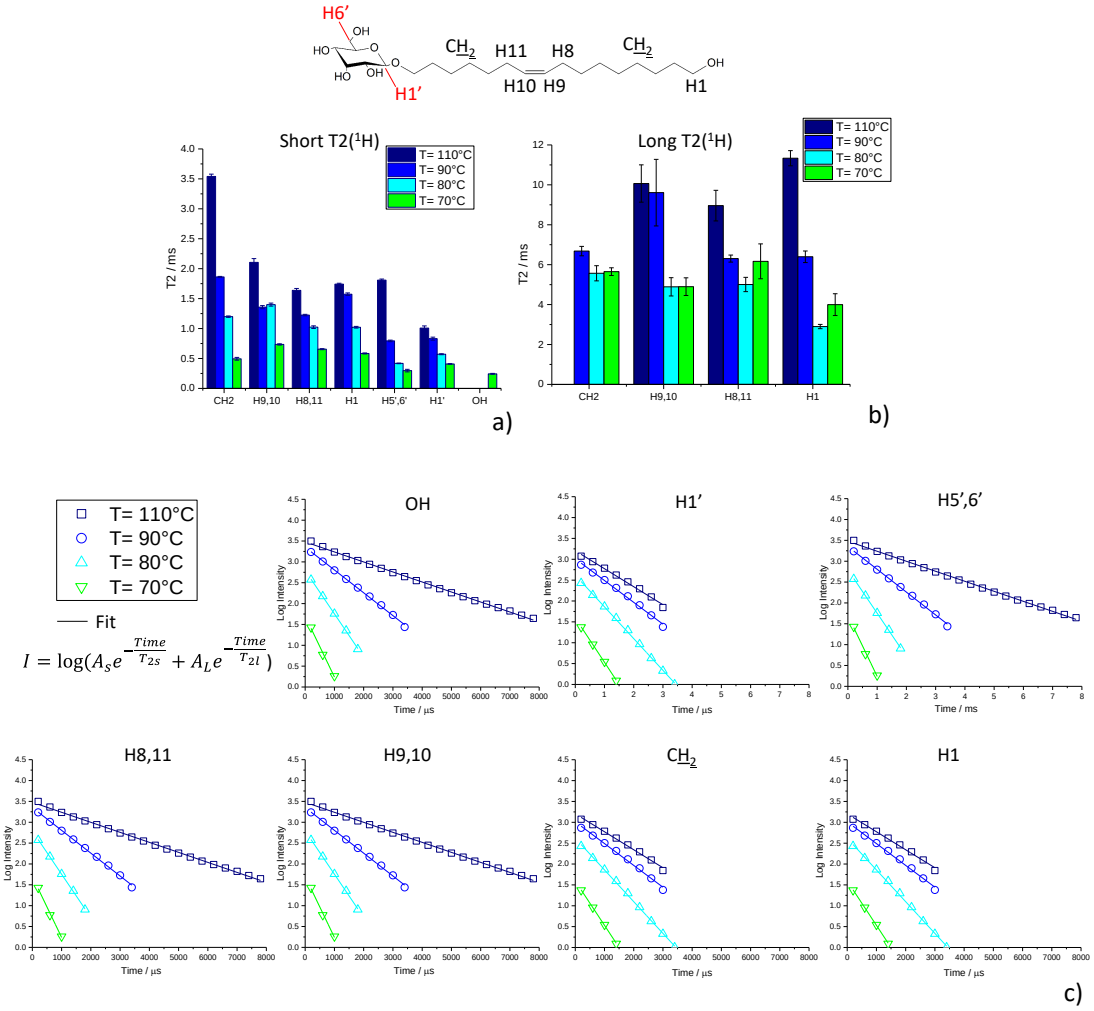

Figure S 8 – a) Short and d) long T_2 components displayed by the ^{1}H transverse relaxation signal. c) ^{1}H transverse relaxation signals recorded on a G-C18:1-OH dry powder from 110°C to 70°C. The area of each given resonance is plotted (log-lin) as a function of the echo time (CPMG pulse sequence) for each temperature and fitted using the equation given above. T_{2s} and T_{2l} indicate the short and long T_2 relaxation times respectively obtained by describing the ^{1}H transverse relaxation signal using a biexponential decay. For H1', H5' and H6', the ^{1}H relaxation function could be described by a monoexponential decay.

- Protons from the sugar group (H1', H5', H6') show a single T_2 relaxation component (Figure 6c and Figure S 8), while protons of the acyl chain (C<u>H</u>$_2$, H9,10, H8,11) show both short (Figure 6c) and long (Figure 6d) T_2 relaxation component.

- The short T_2 relaxation time systematically decreases from 110°C to 70°C for all species by a factor ranging from two to seven, depending on the specific chemical group. Very long T_2 are observed at 110°C for all acyl species, while nearly unchanged values are measured below 90°C, without any clear trend.

- The sugar protons (H1', H5', H6') have the shortest set of T_2 values (< 1 ms) below 100°C. The long component of T_2 generally ranges between 4 ms and 12 ms.

Table S 1 – ^{1}H chemical shifts of G-C18:1-OH in solution and in the solid-state. Solid-state spectra are recorded at a MAS frequency of 10 kHz. *: in DMSO-d6 ; #: broad peak.

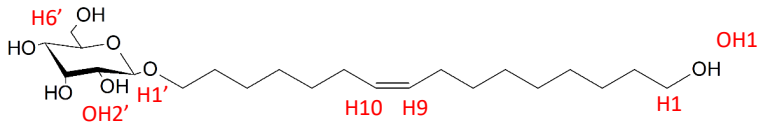

		δ_H / ppm		
Group	N°	Liquid (MeOD-d4)	Solid (*T*= 110°C)	Solid (*T*= 70°C)
CH_2	H1	3.54	3.57	
CH_2	H2	1.53	1.56	
CH_2	H3-7/12-14	1.32	1.35	
CH_2	H8,11	2.03	2.03	
CH	H9,10	5.34	5.34	
CH_2	H15	1.62	1.64	
CH_2	H16	3.88	3.83	
CH	H1'	4.24	4.32	
CH	H2'	3.16	3.35	
CH	H3'	3.34	3.35	
CH	H4'	3.29	3.35	
CH	H5'	3.54	3.51	3.57
CH_2	H6'	3.66	3.83	
OH*	OH1	4.32	4.5#	4.63
OH*	OH2'	4.92		
OH*	OH3'	4.90		
OH*	OH4'	4.87		
OH*	OH6'	4.45		

Detailed discussion about the NOESY and DQ-SQ 2D ^{1}H-^{1}H ssNMR experiments presented in Figure 9

2D ^{1}H-^{1}H ssNMR experiments are a unique tool to explore through-space proximities between ^{1}H nuclei. ssNMR offers a large number of possibilities, each adapted to a given system. The advantage of 2D maps with respect to a dynamics approach is their direct readability; in clear, two nuclei which exchange their magnetization through-space (whichever mechanism may be responsible for this exchange) will display a specific cross-peak. However, the way cross-peaks are presented and interpreted strictly depends on the nature of the pulse program, which in turn is chosen according to the physical nature of the sample.

1D, temperature-dependent, ^{1}H NMR experiments performed on G-C18:1-OH (Figure 4a in the main text) indicate sharp peaks at 90°C and broad peaks at 70°C. Narrow peaks indicate fast and/or large-amplitude molecular tumbling, averaging the strong ^{1}H-^{1}H dipolar interactions. This excludes the use of pulse sequences, like DQ-SQ, which is not efficient under these conditions. For this reason, we employ spin-diffusion-based pulse sequences, like NOESY, which is more adapted for samples with high molecular mobility. When mixing times are chosen to be short (< 1 s), one generally explores through-space proximities within about 5 10 Å. On the contrary, when molecular motions are restricted, dipolar coupling becomes significant, ^{1}H NMR peaks are broader and pulse sequences, like DQ-SQ, can now be used, with a spatial resolution of less than 5 Å.

Whenever possible, DQ-SQ experiments are preferred over spin diffusion-based pulse sequences, because they are more selective, in particular for likewise interactions, which are not discriminated in NOESY-type experiments. This is illustrated by the typical interaction schemes for NOESY (top Figure 9a) and DQ-SQ (top Figure 9b). For two given A and B protons, 2D NOESY maps will display two on-diagonal and two square-shaped symmetrical off-diagonal cross-peaks. Off-diagonal cross-peaks illustrate the mutual A-B and B-A interaction, but the on-diagonal peaks are systematic and do not prove any A-A or B-B interaction. Similarly to NOESY, 2D DQ-SQ maps display off-diagonal peaks (symmetric across the diagonal, top Figure 9b) upon A-B and B-A interaction, but in contrast they will display on-diagonal peaks only in the presence of self-interaction. In the tutorial example of Figure 9b top, the on-diagonal A-A peak indicates mutual A-A interaction while lack of on-diagonal B-B peak evidences the absence of B-B proximities. Combining NOESY and DQ-SQ experiments is capital to study the local arrangement of G-C18:1-OH and its evolution with temperature.

At T= 90°C, the H1 and H5’ contributions are very close but possible to discriminate them (δ(H1)= 3.54 ppm, δ(H5’)= 3.51 ppm) according to ^{1}H NMR chemical shifts in Table S 1. 2D ^{1}H-^{1}H NOESY in Figure 9a also discriminates between the two components, attributed on the basis of the interactions with their mutual neighbors (green H1-H2 and H5’-H1’ squares in Figure 9a). On this basis, 2D NOESY does not show a direct H1’-H1 correlation (blue, red-crossed), but rather an extensive network of intra-sugar interactions. These features exclude suggest intra- and inter-sugar interactions and they exclude head-tail arrangements as a major molecular configuration at 90°C.

At 70°C, the ^{1}H NMR peaks are broader, indicating a reduction of the T_2 (^{1}H) relaxation times and/or residual homonuclear dipolar interactions, excluding the use of NOESY. In this case, ^{1}H-^{1}H DQ-SQ correlation experiments are best suited. Figure 9b presents the ^{1}H-^{1}H DQ-SQ experiment on G-C18:1-OH at 70°C. Peaks are broader than in NOESY and attribution may be cumbersome. However, the experiment is performed at 700 MHz and MAS= 22 kHz, which improves spectral resolution with respect to the same experiment performed at 300 MHz and MAS= 10 kHz. The auto-peak at δ_H= 3.56 ppm in the SQ dimension is attributed to H1-H1 spin pairs, mainly resulting from intra CH_2 interaction, while the DQ cross-peaks at δ_H= 1.56-3.56 ppm and δ_H= 4.32-3.56 ppm respectively origin from H2-H1 and H1’-H1 interactions (Figure 9b). DQ-SQ map does not show any auto-peak corresponding to H1’-H1’ or Hx’-Hx’ (x= 2’, 3’, 4’) interactions (red-crossed, blue, Figure 9b), thus excluding any proximity (< 5 Å) between close glucose neighbors. On the contrary, DQ-SQ maps (recorded both at 700 MHz, Figure 9b, or at 300 MHz, not shown) systematically show DQ cross-peaks, which can only be attributed to H1’-H1 interactions (δ_H= 4.32-3.56). The presence of these H1’-H1 interactions can only be explained by a head-tail arrangement of the G-C18:1-OH molecules, as illustrated below the DQ-SQ map in Figure 9b.